GeroScience (2024) 46:3481–3501
https://doi.org/10.1007/s11357-024-01090-7

ORIGINAL ARTICLE

Vascular smooth muscle cell-specific Igf1r deficiency exacerbates the development of hypertension-induced cerebral microhemorrhages and gait defects

Lauren R. Miller · Marisa A. Bickel · Michaela L. Vance · Hannah Vaden · Domonkos Nagykaldi · Adam Nyul-Toth · Elizabeth C. Bullen · Tripti Gautam · Stefano Tarantini · Andriy Yabluchanskiy · Tamas Kiss · Zoltan Ungvari · Shannon M. Conley

Received: 5 December 2023 / Accepted: 3 February 2024 / Published online: 23 February 2024

Abstract Cerebrovascular fragility and cerebral microhemorrhages (CMH) contribute to age-related cognitive impairment, mobility defects, and vascular cognitive impairment and dementia, impairing healthspan and reducing quality of life in the elderly. Insulin-like growth factor 1 (IGF-1) is a key vasoprotective growth factor that is reduced during aging. Circulating IGF-1 deficiency leads to the development of CMH and other signs of cerebrovascular dysfunction. Here our goal was to understand the contribution of IGF-1 signaling on vascular smooth muscle cells (VSMCs) to the development of CMH and associated gait defects. We used an inducible VSMC-specific promoter and an IGF-1 receptor (Igf1r) floxed mouse line (*Myh11-Cre^{ERT2} Igf1r$^{f/f}$*) to knockdown Igf1r. Angiotensin II in combination with L-NAME-induced hypertension was used to elicit CMH. We observed that VSMC-specific Igf1r knockdown mice had accelerated development of CMH, and subsequent associated gait irregularities. These phenotypes were accompanied by upregulation of a cluster of pro-inflammatory genes associated with VSMC maladaptation. Collectively our findings support an essential role for VSMCs as a target for the vasoprotective effects of IGF-1, and suggest that VSMC dysfunction in aging may contribute to the development of CMH.

Supplementary Information The online version contains supplementary material available at https://doi.org/10.1007/s11357-024-01090-7.

L. R. Miller · M. A. Bickel · M. L. Vance · H. Vaden · D. Nagykaldi · E. C. Bullen · S. M. Conley (✉)
Department of Cell Biology, University of Oklahoma Health Sciences Center, 940 Stanton L. Young Blvd, BMSB 553, Oklahoma City, OK 73104, USA
e-mail: Shannon-conley@ouhsc.edu

L. R. Miller
Currently at: Cardiovascular Biology Research Program, Oklahoma Medical Research Foundation, Oklahoma City, OK 73104, USA

A. Nyul-Toth · T. Gautam · S. Tarantini · A. Yabluchanskiy · Z. Ungvari · S. M. Conley
Vascular Cognitive Impairment and Neurodegeneration Program, Oklahoma Center for Geroscience and Healthy Brain Aging, University of Oklahoma Health Sciences Center, Oklahoma City, OK 73104, USA

A. Nyul-Toth · T. Gautam · S. Tarantini · A. Yabluchanskiy · Z. Ungvari
Department of Neurosurgery, University of Oklahoma Health Sciences Center, Oklahoma City, OK 73104, USA

A. Nyul-Toth · Z. Ungvari
International Training Program in Geroscience, Doctoral School of Basic and Translational Medicine/Department of Public Health, Semmelweis University, Budapest, Hungary

S. Tarantini · Z. Ungvari
The Peggy and Charles Stephenson Cancer Center, University of Oklahoma Health Sciences Center, Oklahoma City, OK, USA

Keywords Insulin-like growth factor 1 · Cerebral microhemorrhage · Aging brain · Vascular cognitive impairment · Vascular smooth muscle cells · Cerebrovascular aging

Introduction

Cerebrovascular pathologies in aging contribute to impairments in cognition and motor function that reduce healthspan and quality of life in elderly individuals [1–4]. Cerebral microhemorrhages (CMHs, also called cerebral microbleeds) originate from the rupture of brain microvasculature, typically arterioles and capillaries measuring < 200 μm in diameter [5, 6]. CMH measure < 5 mm in diameter in humans and can be visualized on T2*-weighted gradient-recall echo (GRE) or susceptibility-weighted imaging (SWI) MRI sequences as round, hypointense regions [7–9]. Two major risk factors for developing CMH have been identified: age (> 65 years of age) and hypertension [10, 11]. Though once thought to be subclinical, the presence of multiple CMH in patients is associated with the development of cognitive decline [12, 13] and gait defects [14, 15]. CMHs are also correlated with Alzheimer's disease (AD) and ischemic and hemorrhagic stroke with a greater prevalence of CMHs reported in patients with recurring strokes [8, 9, 16]. We are interested in the cellular mechanisms that contribute to vascular fragility and the development of CMH in aging.

Vascular smooth muscle cells (VSMCs) are the contractile cells of large- and medium-sized blood vessels (arteries, arterioles, venules, and veins) and are essential for proper vascular stability and vascular responses to hypertension and blood pressure variations. In response to a vascular injury, growth factors, or other environmental stressors such as hypertension, inflammation, and vascular injury, VSMCs can adopt many different phenotypes. These include protective phenotypes characterized by hypertrophy and expression of ECM remodeling genes [6, 17, 18], and maladaptive phenotypes which can contribute to vascular calcification, pathological vascular remodeling [19], and fragility-associated conditions such as intracranial aneurysms [20]. Insulin-like growth factor 1 (IGF-1) is a pleotropic growth hormone with vasoprotective effects, many of which are exerted through its action on VSMCs [13, 21]. For example, IGF-1 treatment of microvascular VSMCs can lead to increased expression of ECM remodeling genes and stimulate VSMC proliferation in the aortas of a diabetic rat model [22, 23]. These IGF-1-mediated protective effects in VSMCs also play a role in vascular diseases. IGF-1 is protective in atherosclerosis due to effects on multiple cell types, including VSMCs, where the effects of IGF-1 promote plaque stability [24–26].

Levels of IGF-1 decrease with increasing age in humans and animal models [21, 27–30], and circulating IGF-1 deficiency leads to accelerated development of many age-related cerebrovascular pathologies in animal models [31–42]. These include impaired neurovascular coupling, microvascular rarefaction, and impaired myogenic autoregulation (a function largely carried out by VSMCs), and other vascular pathologies [38, 40, 43, 44]. Critically, circulating IGF-1 deficiency is also associated with impaired vascular remodeling in response to hypertension and the development of signs of vascular fragility such as CMH [7, 34].

Here, we were interested in understanding whether reduced IGF-1 signaling on VSMCs increased susceptibility to CMH and subsequent gait deficits. We utilized a VSMC-specific IGF-1 receptor (Igf1r) knockdown model to evaluate the development of hypertension-induced CMH. We found that VSMC-specific Igf1r deficiency leads to accelerated CMH formation and gait impairments. Our findings demonstrate a critical role for VSMCs in IGF-1 deficiency-related CMH occurrence.

Materials and methods

Animal model

All animal experiments and husbandry activities were approved by the Institutional Animal Care and Use Committee at the University of Oklahoma Health

S. Tarantini
Department of Health Promotion Sciences, College of Public Health, University of Oklahoma Health Sciences Center, Oklahoma City, OK, USA

T. Kiss
Pediatric Center, Semmelweis University, Budapest, Hungary

T. Kiss
Eötvös Loránd Research Network and Semmelweis University Cerebrovascular and Neurocognitive Disorders Research Group, Budapest, Hungary

Sciences Center (IACUC; University of Oklahoma Health Sciences Center, OK, USA). The inducible vascular smooth muscle cell-specific IGF-1 receptor (Igf1r) knockdown mice were created using a mural cell-specific Cre recombinase *Myh11-Cre^{ERT2}* (B6. FVB-Tg(Myh11-icre/ERT2)1Soff/J, Strain #:019079) bred with the *Igf1r$^{f/f}$* line (B6;129-Igf1rtm2Arge/J, Strain #:012251). We additionally crossed these animals onto a tdTomato lineage tracer line (*ROSA$^{f/f\ tdT}$* B6.Cg-Gt(ROSA)26Sortm9(CAG-tdTomato)Hze/J, Strain #:007909) to generate *Myh11Cre^{ERT2} ROSA$^{f/f\ tdT}$ Igf1r$^{f/f}$* in which Cre-mediated excision in these cells allowed for life-long expression of the tdTomato fluorophore as well as downregulation of the Igf1r protein (although no experiments utilizing the reporter are included in this study). Genotyping primers are listed in Table S1. Control animals were age-matched *Myh11-Cre^{ERT2} ROSA$^{f/f\ tdT}$ Igf1r$^{+/+}$* mice. Cre induction was done at 4 months of age with tamoxifen (75 mg/kg over 5 consecutive days; Millipore Sigma, St. Louis MO, USA) to allow for proper development prior to knockout. Only male mice were used for these experiments as the *Myh-11Cre^{ERT2}* transgene resides on the Y-chromosome. Animals used in these studies were 10–12 months of age. Mice were housed in pathogen-free barrier conditions in the OUHSC Rodent Barrier Facility. Before mini-pump implantation, mice were moved and acclimated to a conventional rodent housing facility at OUHSC. Mice were on a 12-h light/12-h dark cycle, with access to standard rodent chow (Purina Mills, Richmond, IN, USA) and water ad libitum.

ELISA

Blood was collected from the submandibular vein with a sterile 25-G needle. After coagulating for 20 min at room temperature, the blood sample was centrifuged at 2500 × *g* for 20 min at 4 °C. Serum was collected and stored at − 80 °C until use. Serum IGF-1 was measured by ELISA (R&D Systems, Minneapolis, MN, USA) as previously reported [43]. An IGF-1 control sample was included on each plate. Serum IGF-1 levels were reported in ng mL^{-1}.

Hypertension induction and blood pressure measurements

Hypertension was induced at 10–12 months of age. Igf1r KD and control mice were randomly assigned to either "hypertensive" or "normotensive" experimental groups. Subcutaneous intrascapular osmotic mini-pumps (Alzet Model 2006, 0.15 µL h^{-1}, 42 days; Durect Co, Cupertino, CA, USA) were surgically implanted in isoflurane-anesthetized mice as described previously [38, 45]. The mini-pumps were filled with either sterile saline (for normotensive groups) or angiotensin II (AngII) (Millipore Sigma, 1 µg min^{-1} kg^{-1}) in sterile saline. Buprenorphine extended release (ZooPharm, Fort Collins, CO, USA) was given to alleviate pain post-implantation. Hypertensive mice were also given a nitric oxide synthase inhibitor (L-NAME [N5751, Millipore Sigma], 100 mg/kg·day) in the drinking water as previously described [45]. In some specified experiments, animals only received L-NAME for 3 days post-pump implantation. To ensure hypertension post-surgery, a subset of mice underwent measurement of mean arterial blood pressure (MAP) just prior to euthanasia. Each mouse was anesthetized with ventilated isoflurane, placed on a warming pad, and the femoral artery was surgically cannulated. The cannula was then attached to blood pressure monitors and MAP was recorded. Each mouse was then euthanized by cardiac perfusion under anesthesia.

Standardized neurological examination and removal criteria

Mice underwent daily neurological examinations starting at day 3 post-pump implantation until the endpoint of the experiment. The neurological scoring system uses an 18-point scale that assesses body proprioception, vibrissae touch response, symmetry in limb movement, forelimb outstretching, climbing ability, and spontaneous activity [7, 45]. A decline in neurological score to 17 indicates the development of CMH and is the desired experimental endpoint for assessment of CMH. A decline in neurological score to 15 or below is indicative of hemorrhagic stroke and is the humane endpoint [45, 46]. At the study endpoint, defined as the day a drop in neurological score was detected or day 21 in animals that did not exhibit a drop in neurological score, mice were transcardially perfused under either isoflurane or ketamine/xylazine (85 mg/kg/14 mg/kg) anesthesia with ice-cold 1 × phosphate buffered saline (1 × PBS, 137 mM NaCl, 2.7 mM KCl 10 mM Na_2HPO_4, 1.8 mM KH_2PO_4, pH 7.2–7.4) for 10 min prior to tissue harvest.

Histological analysis of cerebral microhemorrhages

Brains were collected from transcardially perfused mice and fixed in 4% paraformaldehyde for 48 h at 4 °C and stored in PBS at 4 °C until they were embedded in paraffin. Serial coronal brain sections were cut at 8 µm thickness across the entire brain. All slides were stained with 3,3-diaminobenzidine (DAB) (Vector Laboratories/Maravai LifeSciences, San Diego, CA, USA) to reveal hemorrhages, and counterstained with Gill's No. 1 hematoxylin (Millipore Sigma) to show brain structure. DAB reacts with endogenous peroxidases in red blood cells generating a dark brown product that allows for easy and precise detection of extravasated blood in the brain parenchyma. Brain sections were imaged at 10 × using the VS120-L100-W Virtual Slide Microscope (Olympus Life Science, Center Valley, PA, USA).

Microbleed area analysis

CMH in DAB-stained images were analyzed in every 10th coronal section (~80 µm apart). Microbleeds were identified and extracted manually by observers blinded to treatment and genotype from each selected coronal section using Adobe Photoshop CS6 (v.13.0). These extracted images were then processed through a validated custom Fiji (v.1.54e 4 June 2023) script as described previously [46]. The extracted images were read into Fiji and underwent color deconvolution, bandpass filter processing, and application of an automatic thresholding algorithm to generate a binary mask of the bleed. The bleed area, perimeter, and other shape descriptors from ImageJ (i.e., aspect ratio, circularity) were collected. Results were compiled and analyzed in Microsoft Excel. At the time of analysis, the anatomical region of the bleed was manually annotated using the Allen Brain Atlas (https://mouse.brain-map.org/static/atlas, last accessed 11/14/2023) [47]. Minimum CMH size was defined as 26.4 µm^2 (the approximate cross-sectional area of a single red blood cell). All bleeds greater than that size were included in the analysis. CMH were defined as a maximum size of ~300 µm in diameter (70,000 µm^2) based on prior studies [48].

Gait analysis

Gait analysis was performed using the CatWalk Gait Analysis System (Noldus Information Technology, Inc., Leesburg, VA, USA) as described previously [7, 49, 50]. Experimenters and analyzers were blinded to the genotype and treatment of each mouse. The mice were acclimated to the CatWalk for 5 min in a dimly lit room intended for behavioral assessments for 1–2 days before the start of the experiment. Five voluntary runs were acquired for each mouse on each measurement day. The day before mini-pump implantation, a baseline measurement was recorded for each animal. Measurements were then recorded daily for each animal starting on post-surgery day 3 until the day each animal was euthanized (when the neurological score dropped below 18 or on post-surgery day 21). The footprints from the recorded video files were then classified by a blinded observer, and classified runs were then analyzed for various parameters, including regularity index, front and hind base of support (BOS), stride length, duty cycle, and swing speed [7, 46]. Footfall patterns were also assessed for the percentage of normal versus rare patterns (Table S2) [49].

Stride length is the distance between the displacement and successive replacement of a single paw (measured in cm). *Front and hind BOS* are the distance between the animal's two front or hind paws (measured in cm), respectively. *Regularity index* is a measure of inter-paw coordination that assesses the amount of normal step sequence patterns as compared to the total number of paw placements. Mice with no gait deficits should have a regularity index close to 100%. The regularity index is calculated as follows:

$$Regularityindex(\%) = \frac{\#ofnormalstepsequencepatterns \times 4}{Total\#ofpawplacements} \times (100\%)$$

Duty cycle compares the amount of time that an animal is on one foot (stand) as a function of the length of the entire step cycle for that foot (the time that the foot is on the ground in combination with the time that the foot is in the air). Duty cycle is calculated as follows:

$$Dutycycle(\%) = \frac{Stand(\mathrm{s})}{Stand(\mathrm{s}) + Swing(\mathrm{s})} \times (100\%)$$

Swing speed is the speed of each paw during the swing (the period of time in which the paw does not come in contact with the glass in the CatWalk apparatus). Swing speed is calculated as follows:

$$Swingspeed(\mathrm{cm/s}) = \frac{Stridelength(\mathrm{cm})}{Swing(\mathrm{s})}$$

Protein isolation and western blots

Protein isolation and western blots were performed as previously described [70]. Protein was extracted from flash frozen aortas that were manually pulverized and placed in lysis buffer (10 mMTris-HCl pH 7.6, 1.0% Triton X-100, 100 mM NaCl, 2.0 mM EDTA, 10% v/v glycerol, 50 mM NaF, 20 mM $Na_4P_2O_7$, 2.0 mM Na_3VO_4, and 1×protease inhibitor cocktail [Roche Complete, EDTA-free protease inhibitor cocktail, Millipore Sigma]). Samples were sonicated and then incubated on a rocking platform at 4 °C for 30 min. Insoluble material was removed by centrifugation at 15,000×*g* for 10 min at 4 °C and protein was quantified using Bradford reagent (Bio-Rad, Temecula, CA, USA). SDS-PAGE and western blots were performed according to standard protocols. Blots were incubated overnight in primary antibody: rabbit anti-Igf1r at 1:500 (Cat# 182408, Abcam, Waltham, MA, USA). After washing, blots were incubated with secondary antibody: goat anti-rabbit 800 used at a dilution 1:1000 (Licor Biosciences, Lincoln, NE, USA). β-actin-HRP antibody (1:10,000, Cat# A3854, Millipore Sigma) was used as a loading control. Blots were imaged using a Licor Odyssey Fc imager (Licor). Densitometric analysis of blots with unsaturated bands was performed with Image Studio (Version 5.2, Licor).

Analysis of gene expression

Hippocampus and cerebral cortex were dissected and flash frozen in liquid nitrogen. Hippocampus and cerebral cortex samples were sonicated, and total RNA was isolated using RNeasy Mini QIAcube Kit according to the manufacturer's instructions (cat. no. 74116, Qiagen, Germantown, MD, USA). RNA concentration and purity were measured using a DeNovix DS-11 spectrophotometer. Total RNA was reversed transcribed into cDNA using the High-Capacity RNA-to-cDNA Kit according to the manufacturer's instructions (cat. no. 4387406, Applied Biosystems ThermoFisher) using a Bio-Rad T100 thermocycler (Bio-Rad). A TaqMan Gene Expression Custom Array Card was designed to test 96 qPCR targets each associated with response to CMH (cat. no. 4342259, Applied Biosystems ThermoFisher). Each port of a microfluidic card was loaded with 100 µl of reaction mixture per manufacturer's instructions using TaqMan Universal Master Mix II with UNG (cat. no. 4440038, Applied Biosystems ThermoFisher) and 10 µl of cDNA. Each card included one sample from each experimental group. Cards were centrifuged at 2200 rpm for 1 min prior to sealing and excising ports. qPCR was performed using the QuantStudio 12 K Flex Real-Time PCR System.

Analysis of qPCR data was carried out in Python (v.3.9). Initial screening was used to exclude genes with more than two missing C_t values. The stability of control genes was assessed utilizing NormFinder [51]. The two most stable control genes were determined separately for cortex (*B2m* and *Ywhaz*) and hippocampus samples (*Gapdh* and *Hprt*). Normalization of qPCR data was performed utilizing the geometric mean of the selected control genes [52]. All plots were created using Graphpad Prism version 9.2. Two-way ANOVA was performed by the stats (v.4.2.1) package aov function.

Statistical analysis

Statistical analyses were performed using Graphpad Prism version 9.2 unless otherwise noted. Unpaired *t*-tests or Mann–Whitney *U* tests (depending on normality of data) were used when only two samples were compared, one-way ANOVA with Tukey's post hoc test was used when three or more samples were analyzed, and two-way ANOVA with Tukey's post hoc test was used when multiple variables were included (i.e., genotype and hypertension status). Comparisons of survival curves were performed using Kaplan–Meier analysis. Data are presented as mean ± SEM or median ± 95% confidence interval as indicated in figure legends. Significance was set at $p < 0.05$. Two-way repeated measures ANOVA was used to compare baseline to last day gait measurements (with Tukey's post hoc test). *F*-test was used to test whether variances were equal. *P*-values presented underneath graphs represent *P*-values

from two-way ANOVA. When pairwise comparisons were significant, they are marked on graphs with individual brackets.

Results

VSMC-specific Igf1r deficiency accelerates the development of cerebral microhemorrhages

To investigate the role of VSMCs in the development of CMHs associated with IGF-1-deficiency, we used a mouse model of VSMC-specific Igf1r-knockdown (*Myh11Cre*^{ERT2} *Igf1r*$^{f/f}$, hereafter referred to as Igf1r KD) and controls (*Myh11Cre*^{ERT2} *ROSA*$^{f/f\ tdT}$ *Igf1r*$^{+/+}$). Tamoxifen-mediated knockdown of Igf1r was induced at P120 (Fig. 1A) to allow for full development prior to interfering with the IGF-1 axis. To confirm knockdown, we assessed Igf1r levels in the VSMC-rich aorta at 1 year of age. We observed ~ 60% knockdown of Igf1r levels in Igf1r KD aortas (Fig. 1B, C) while circulating IGF-1 levels were not different between Igf1r KD and controls (Fig. 1D).

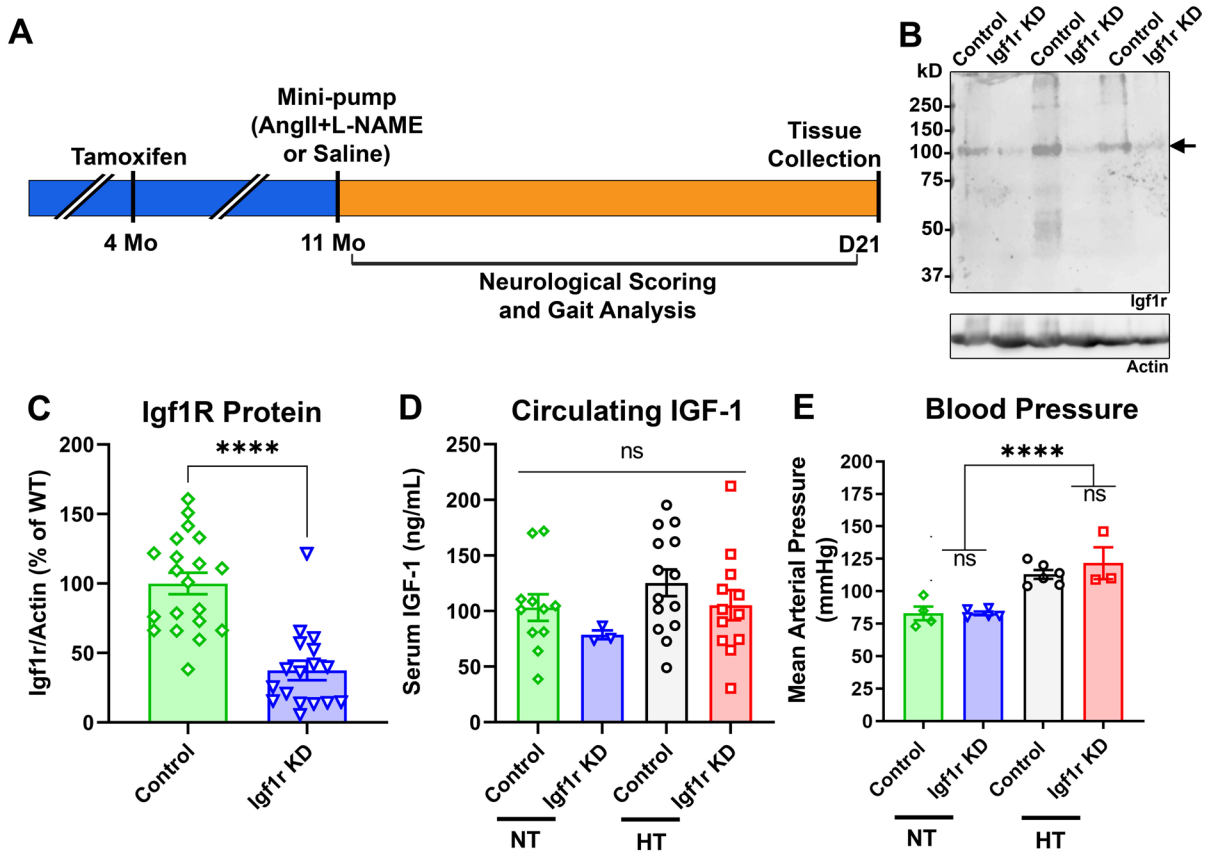

Fig. 1 VSMC-specific Igf1r KD model: **A**. Experimental paradigm for the Igf1r knockdown mouse model. **B** and **C**. Igf1r knockdown was confirmed by western blot of aortic protein extracts collected at 1 year of age in control ($n = 20$) and Igf1r KD ($n = 17$) normotensive (NT) mice. Igf1r is present ~ 100 kDa (arrow). Densitometry signal was normalized to β-actin levels. Igf1r KD animals had lower levels of Igf1r protein than their control counterparts (****$P < 0.0001$ by Mann–Whitney *t*-test). **D**. Serum IGF-1 levels were evaluated by ELISA (ns: not significant by two-way ANOVA with Tukey's post hoc test) in control ($n = 11$) and Igf1r KD ($n = 3$), normotensive and control ($n = 14$), and Igf1r KD ($n = 12$) hypertensive (HT) mice. **E**. Mean arterial blood pressure was measured immediately prior to euthanasia ($n = 4$, control normotensive; $n = 5$, Igf1r KD normotensive; $n = 6$, control HT; $n = 3$, Igf1r KD HT). Combined treatment with AngII and L-NAME successfully increased mean arterial blood pressure in both control and Igf1r KD mice (****$P < 0.0001$, two-way ANOVA, with Tukey's post hoc comparison). All graphs show mean ± SEM

To elicit CMH, we used an established paradigm in which hypertension was induced using a combination of angiotensin II (infused by osmotic mini-pump) coupled with provision of L-NAME in the drinking water to cause blood pressure spikes (Fig. 1A) [50]. Normotensive mice received no L-NAME and mini-pumps contained saline. Hypertension was induced at ~ 10–12 months of age (Fig. 1E), an established time point used in studies evaluating IGF-1 deficiency as an accelerated aging model [7, 38]. After the induction of hypertension, mice underwent twice daily neurological scoring. A consistent drop in score reflects the development of CMH and was the study removal criterion. Igf1r knockdown (KD) hypertensive mice had a significantly earlier onset of neurological signs of CMH (i.e., drop in neurological score) than hypertensive controls as reflected in both incidence curves and the mean number of days until neurological decline was detected (Fig. 2A, B). As expected, normotensive animals had no change in neurological score.

To assess the number, size distribution, and location of CMHs histologically, a subset of hypertensive brains harvested on the day a drop in neurological score was detected were serially sectioned and DAB stained (brown region in Fig. 2C is a CMH). Bleeds were manually identified in sections taken every 80 µm through the brain and bleed area was analyzed using a series of processing steps in ImageJ (Fig. 2C) as described previously [46]. There was a trend towards increased

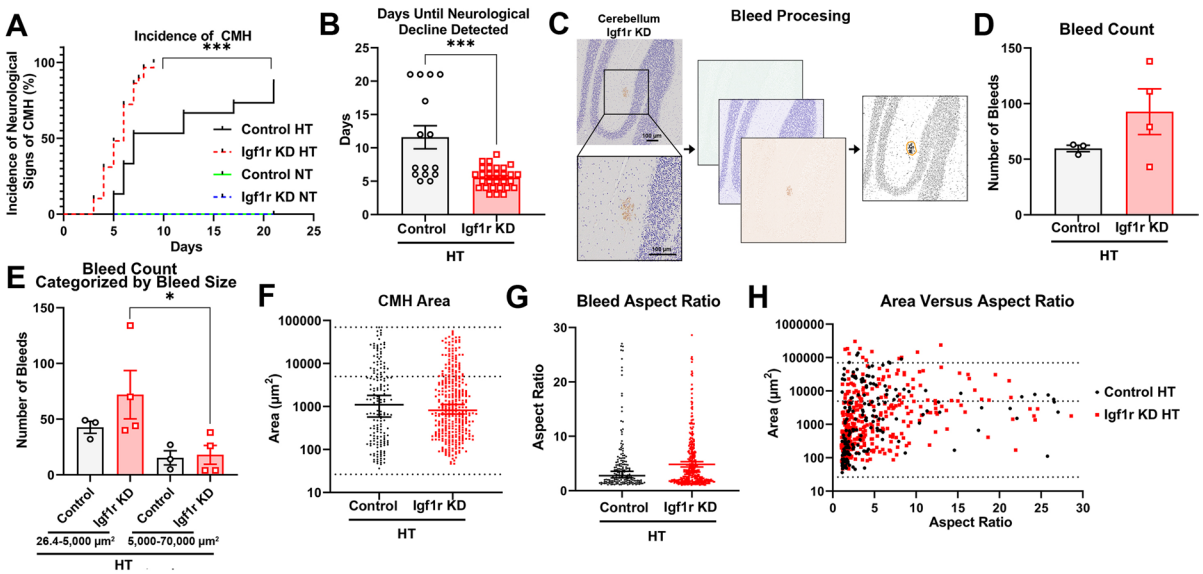

Fig. 2 VSMC-specific Igf1r KD accelerates development of CMH: 10–12-month-old Igf1r KD and control mice were implanted with mini-pumps containing saline (NT: normotensive) or angiotensin II (HT: hypertensive) (pump implantation was day 0) and given drinking water supplemented with L-NAME. **A**. Incidence curves plotting incidence of neurological signs of CMH. Igf1r KD HT mice experienced an earlier onset of neurological signs than control HT mice (incidence curves were compared using Kaplan–Meier analysis, $***P<0.001$, $n=15$ control HT, $n=29$ Igf1r KD HT, $n=9$ control NT, $n=12$ Igf1r KD NT, sample sizes the same for B). **B**. Igf1r KD mice developed signs of CMH significantly sooner than controls ($***P<0.001$ by Mann–Whitney test). **C**. Serially sectioned brains from HT Igf1r KD and control animals were DAB stained (brown) and counterstained for nuclei (blue). Shown are images from the Fiji script used to analyze bleeds and collect metrics. **D**. Plotted is total number of bleeds per brain (Igf1r KD $n=4$ animals, control $n=3$) **E**. Bleed number was subgrouped into small bleeds (26.4–5,000 µm^2) and large bleeds (5,001–70,000 µm^2). Between-group differences were analyzed using two-way ANOVA followed by Tukey's post hoc comparison, $*P<0.05$. **F**. Plotted is bleed area (µm^2) for individual bleeds in HT Igf1r KD and control animals (displayed as median ± 95% confidence interval since data were not normally distributed). No significant difference was observed between groups ($P=0.8402$ by Mann–Whitney test). **G**. Aspect ratio was analyzed for both HT Igf1r KD and control animals (plotted as median ± 95% confidence interval). No significant difference was observed between groups ($P=0.3825$ by Mann–Whitney test). **H**. Plotted are individual bleed areas as a function of aspect ratio. Except where otherwise noted, graphs plot mean ± SEM

bleed number in Igf1r KD hypertensive vs control hypertensive brains but the difference did not reach statistical significance (Fig. 2D). The variance in bleed number between brains was significantly larger in the Igf1r KD hypertensive group than control hypertensive group ($P = 0.0286$ in F-test to compare variances), suggesting that some Igf1r brains were highly susceptible to bleeds while others were not. To determine whether this variability might be accounted for by neurological score at the time of collection, we plotted bleed number as a function of the final neurological score. Brains were collected as soon as a decline in neurological score was detected, but because some mice decline more rapidly than others, the final neurological scores across our cohorts ranged from 14 to 17. However, we did not observe any correlation between neurological score at the time of collection and the gross number or median area of bleeds (Fig. S1A-B, $r^2 = 0.001693$ for Fig. S1A).

Recent work using a laser-induced CMH model has shown that the size of the CMH strongly correlates with the vessel of origin, with capillary and venular CMH having areas less than ~ 5,000 μm^2 and arteriolar CMH being larger [53]. Based on criteria from murine CMH studies, we defined the maximum size of a CMH to be ~ 300 μm in diameter (70,000 μm^2). When the total number of CMH per brain was split into small (< 5000 μm^2) vs. large (5000–70,000 μm^2), we observed a greater number of small CMHs than large, a difference more pronounced in Igf1r KD vs. control (Fig. 2E), suggesting that capillaries/venules may be more susceptible to rupture in VSMC-specific Igf1r KD mice than arterioles. This was reflected in the observation that median CMH area was lower in Igf1r KD vs. controls (816 μm^2 vs 1101 μm^2), but the wide range of CMH size meant the difference did not reach statistical significance (Figs. 2F and Fig. S2C). We also observe some large bleeds (i.e., not CMH) in both control and Igf1r KD brains (on average 1.6 large bleeds/brain in controls vs. 3 large bleeds/brain in Igf1r KD).

CMH morphology has also been connected to vessel of origin, with capillary CMH being small and spherical, arteriolar CMH larger and spherical, and venular CMH more diffuse, often elongating along in the perivascular space [53]. Morphology can be hard to quantify particularly in bleeds analyzed in single planes (since some bleeds may be expanding perpendicular to the plane of the section). However, one potential metric to quantify morphology is aspect ratio where a higher aspect ratio reflects a more elongated bleed. However, we did not see any significant differences in CMH aspect ratio between Igf1r KD hypertensive and control hypertensive mice (Fig. 2G, H; Fig. S1D). Combined these data indicate that VSMC-specific Igf1r KD mice have significantly earlier onset of hypertension-induced CMH and significantly more variability in the number of CMH per brain compared to hypertensive control mice.

CMH are distributed throughout the brain

To assess spatial distribution of CMH throughout the brain, bleeds were mapped to various brain regions (cortex, cerebellum, hippocampus, olfactory bulb, basal ganglia, white matter, hypothalamus, brainstem, and thalamus) using the Allen Brain Atlas [47]. Bleeds were found throughout the brain, and representative CMH images from Igf1r KD hypertensive mice are displayed in Fig. 3A. In control brains, cortical, hippocampal, and olfactory bleeds comprised 71% of the total bleeds while in Igf1r KD, bleeds were more evenly distributed across multiple regions (Fig. 3B). However, due to variation in bleed location from brain-to-brain, there were no statistically significant differences in bleed distribution between control and Igf1r KD groups (Fig. 3C). The smallest CMH (< 5000 μm^2) exhibited a similar pattern of distribution to the total pool of CMH (Fig. 3 B (right) and D).

VSMC-specific Igf1r deficiency and hypertension lead to the development of gait defects

Gait defects are associated with vascular cognitive impairment and dementia and CMH [54], so we evaluated gait in our cohorts of control and Igf1r KD animals (both hypertensive and normotensive) using the CatWalk Gait Analysis System which permits assessment of freely moving mice. After acclimatizing mice to the CatWalk before the beginning of measurements, a baseline gait measurement was recorded for each mouse on the day before mini-pump implantation surgery. Beginning 3 days after surgery, gait was measured every day until the study removal day (i.e., a decline in neurological score or at post-surgery day 21). After analysis of each CatWalk trial, we compared baseline to final day gait measurements to assess changes in gait.

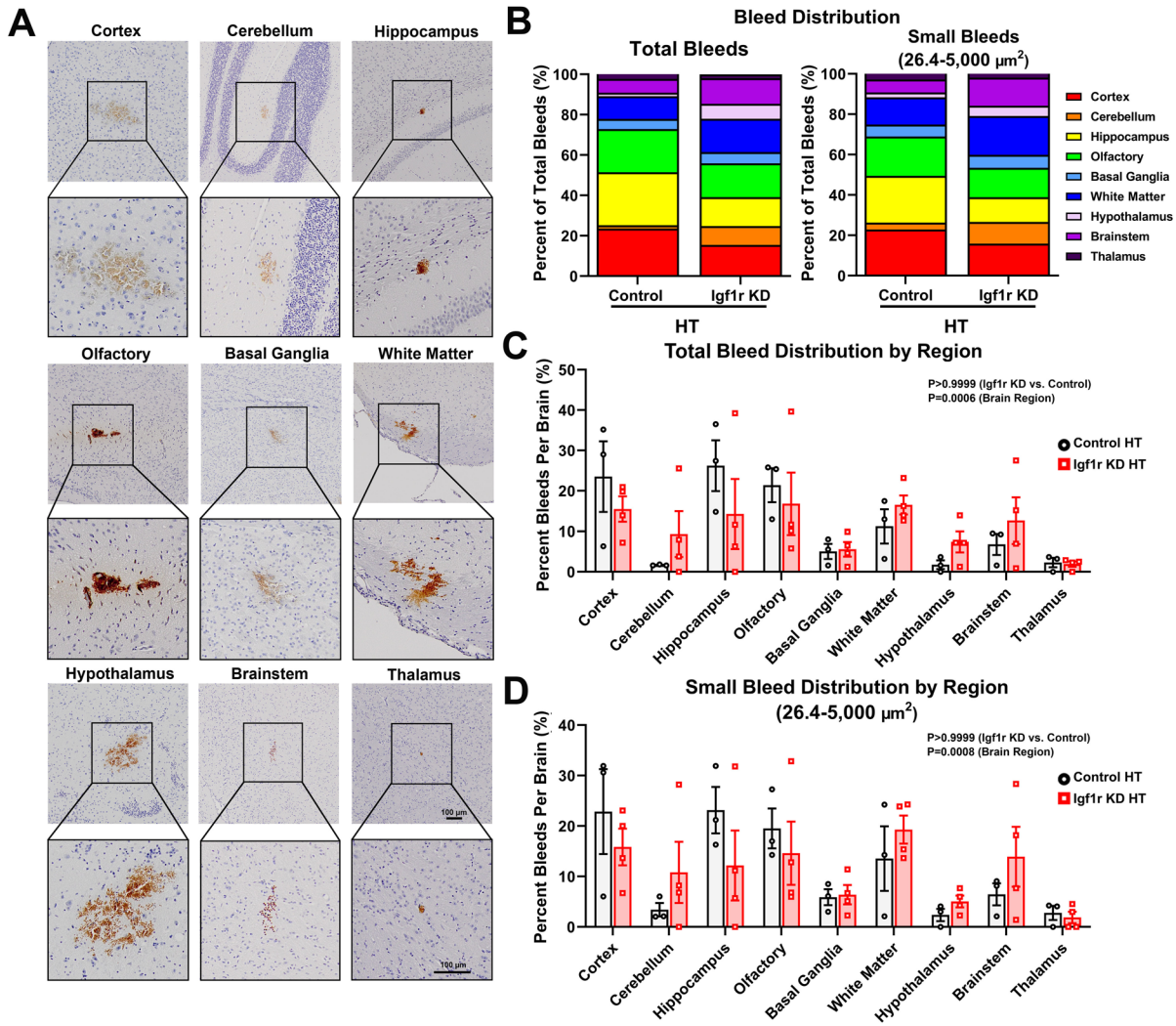

Fig. 3 VSMC-specific Igf1r alters bleed burden and distribution: bleeds from hypertensive Igf1r KD ($n=4$) and control animals ($n=3$) were mapped to nine brain regions (cortex, cerebellum, hippocampus, olfactory bulb, basal ganglia, white matter, hypothalamus, brainstem, and thalamus) to assess changes in bleed distribution across groups. **A**. Example images of bleeds across the nine brain regions from Igf1r KD animals. Scale bars, 100 µm. Boxed areas from top images are blown up above. Brown DAB staining marks CMH. **B–D**. Overall bleed distribution by group is plotted for total bleeds and small bleeds. Plotted are the percentage of total bleeds (C) and small bleeds (D) bleeds found in each region for each brain. Between group differences were analyzed by two-way ANOVA (ANOVA *P*-values were > 0.9999 for Igf1r KD vs. control, $^{***}P<0.001$ for brain region, no pairwise comparisons were significant in post hoc tests)

No gait parameters were altered over the course of the experiment in normotensive control or Igf1r KD animals, suggesting that the mini-pump itself does not significantly affect gait (Fig. 4, green and blue symbols). In contrast, Igf1r KD hypertensive mice exhibited impairment in several spatiotemporal metrics of gait function over the course of the experiment. Hind base of support, the distance between the two hind paws during walking, was modestly but significantly decreased over the course of the study in hypertensive Igf1r KD animals compared to baseline (Fig. 4A), suggesting that there was a decrease in hind stability in Igf1r KD with hypertension. Hind base of support was not changed in other groups, and front base of support was not decreased in any group (Fig. 4B). The related parameters stride length (the

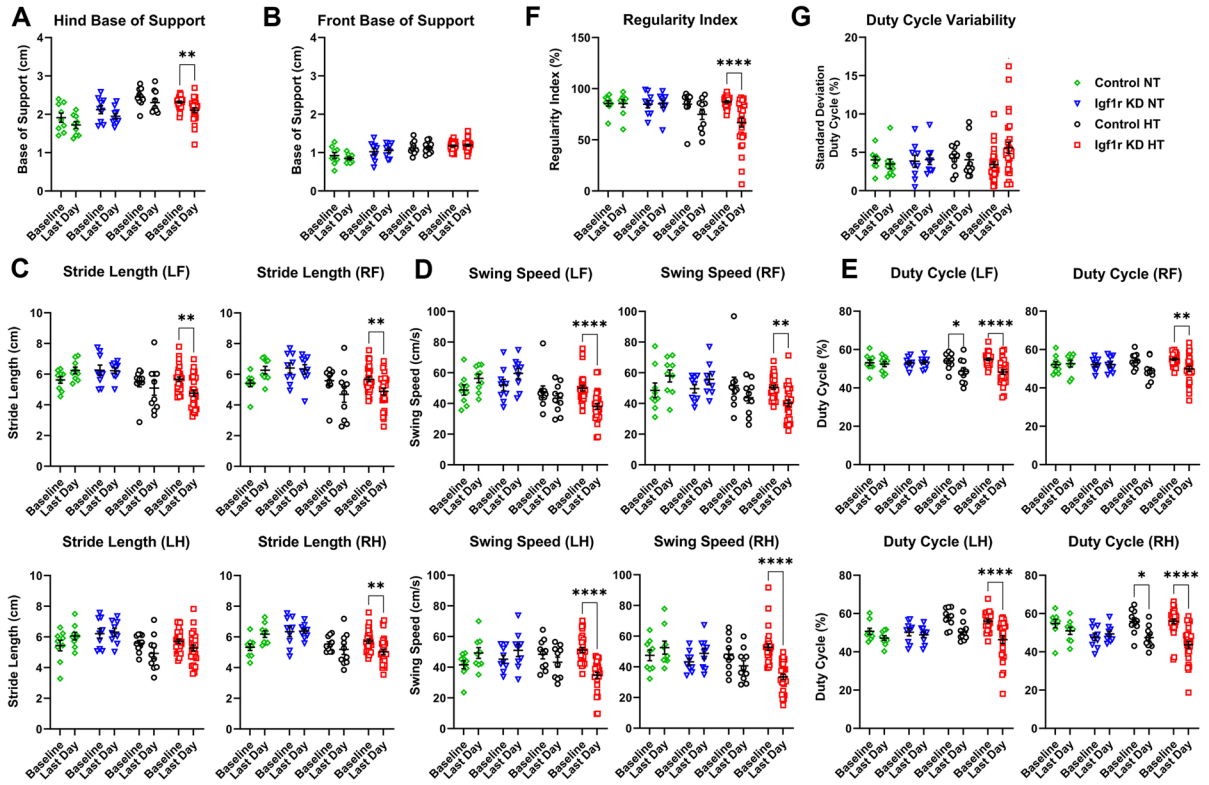

Fig. 4 VSMC-specific Igf1r KD leads to gait defects in the context of CMH: prior to implantation of 10–12-month-old Igf1r KD and control mice with mini-pumps containing saline (NT: normotensive) or angiotensin II (HT: hypertensive), animals underwent baseline gait testing. Starting at day 3 post-pump implantation, animals underwent daily gait testing until removal from the study ($n=9$, control normotensive; $n=9$, Igf1r KD normotensive; $n=10$, control hypertensive; $n=27$, Igf1r KD HT). Plotted are comparisons between baseline measurements and last day (assessed by repeated measures two-way ANOVA followed by Tukey's post hoc tests comparing baseline to last day). $^{*}P<0.05$, $^{**}P<0.01$, $^{****}P<0.0001$. Plotted are various gait metrics, hind, and front base of support (A and B), stride length (C), swing speed (D), duty cycle (E), regularity index (F), and duty cycle variability (G) (mean ± SEM)

distance between the displacement and successive replacement of an animal's paw) and swing speed (stride length divided by swing time) were changed in hypertensive Igf1r KD. Igf1r KD hypertensive mice experienced significantly decreased stride lengths on the last day (compared to baseline) for all limbs except the left hind (LH) limb (Fig. 4C), while swing speeds were reduced in Igf1r KD for all four limbs (Fig. 4D). No changes were seen in other groups. Similarly, we observed significantly decreased duty cycle (the time an animal stands on each paw as a percent of the total step cycle) for all four paws in the Igf1r KD hypertensive group on the last day vs. baseline (Fig. 4E). We also found decreases in duty cycle in two paws (RH and LF) for the control hypertensive group.

In addition to changes in these spatial/temporal metrics, we also observed defects in gait metrics associated with gait symmetry and coordination. Regularity index is a measure of the percentage of footfalls that are part of one of four "regular" footfall patterns (Table S2), and is a fractional measure of inter-paw coordination that has previously been associated with CMH development in mouse models of aging and circulating IGF-1 deficiency [7, 50]. We found that regularity index was significantly decreased in Igf1r KD hypertensive mice (last day compared to baseline), but not in control hypertensive mice (Fig. 4F). Over the course of the experiment, we observed that many mice developed a limp, often neglecting the use of one paw during gait analysis. To quantify this, we calculated duty cycle variability, reflecting

the unevenness in the amount of time a given mouse spent on each foot. Mean duty cycle variability was higher in the Igf1r KD hypertensive group on the last day (vs. baseline) but the difference was not statistically significant (Fig. 4G). However, there was significantly increased population variance in the duty cycle variability metric in Igf1r KD hypertensive on the last day vs. baseline ($P < 0.0001$ in F-test to compare variances) reflecting a high degree of variability within the Igf1r KD hypertensive population in this parameter. Together, these data indicate that hypertension and CMH-associated gait defects are exacerbated in mice with VSMC-specific Igf1r deficiency.

VSMC-specific Igf1r deficiency results in differential expression of genes associated with response to CMH

To help understand what molecular changes might be occurring in the brains during CMH development in Igf1r KD animals, we performed a cross-sectional study evaluating gene expression in cortical and hippocampal tissues harvested 4 days after mini-pump implantation. VSMCs regulate vascular remodeling and injury repair which is an important function that can be activated in response to CMH [55] and hypertension. Using a microfluidic array, we evaluated expression of 96 genes associated with CMH and vascular fragility (Table S3). All genes from this panel that were differentially regulated in response to genotype, blood pressure, or both are displayed in Figs. 5 and Fig. S2 (P-values for two-way ANOVAs are presented under each graph; significant pairwised comparisons are marked on graphs with brackets). We observed a cluster of genes that were similarly upregulated by hypertension in both control and Igf1r KD brains (Fig. S2). These were largely genes that have established anti-fragility phenotypes [7], including ECM components (e.g., *Col4a2, Vcan, Sdc4, Fbln5*) and ECM processing/cross-linking enzymes (e.g., *Plod1, Loxl4, Tgm2, Timp3*) (Fig. S2A-B). Their upregulation in response to hypertension may reflect protective vascular remodeling responses to hypertension and injury. We also observed a cluster of genes that were upregulated in Igf1r KD vs. control independent of whether the mice were hypertensive or normotensive. These include ECM genes such as *Col1a1*, *Col3a1*, *Col12a1*, and *Col18a1*; the proteoglycan decorin (*Dcn*); and the fibulin *Efemp2* (Fig. 5A). There was also a cluster of growth factors that were upregulated in Igf1r KD mice vs. control including *Tgfb2*, *Fgf2*, *Ctgf*, and endothelin 1 (*Edn1*) (Fig. 5B).

Of perhaps most relevance to the development of CMH in our hypertension model, we also observed several genes that were regulated by both hypertension and genotype (Igf1r KD vs control). Most of these genes were upregulated in Igf1r KD hypertensive brains to a much greater degree than Igf1r KD normotensive brains or control brains, though a few were downregulated in Igf1r KD hypertensive brains. Upregulated anti-fragility genes in Igf1r KD hypertensive brains included ECM and ECM cross-linking genes (*Col3a1, Lox, and Loxl2*) and the matrix metalloproteinase (MMP) inhibitor *Timp1*. We also observed that the pro-fragility protease *Adam10* was downregulated in Igf1r KD hypertensive samples (Fig. 5C). Interestingly expression of *Col3a1* was upregulated specifically in Igf1r KD hypertensive cortex samples while it was upregulated in both normotensive and hypertensive Igf1r KD hippocampal tissues. Many other genes were only differentially regulated in one of the two tissues examined (hippocampus or cortex), collectively suggesting that there may be some region-specific regulation.

However, in addition to these anti-fragility changes, we also observed a cluster of pro-fragility gene signatures in Igf1r KD hypertensive mice (vs. control hypertensive or normotensive) brains (Fig. 5D). This includes upregulation of the pro-inflammatory genes *Tnf*, *Sparc*, and *Spp1* which are associated with vascular fragility and aneurysms [56–59]; *Ncf1* which promotes neointima formation in obesity-induced atherogenesis models [60]; and *Cybb* (*Nox2*) which is associated with vascular oxidative stress [61, 62] (Fig. 5D). We also observed hypertension-associated downregulation of some ECM components critical for matrix and basement membrane stability in Igf1r KD including *Col14a1* and *Col16a1* (Fig. 5E).

One challenge is that these tissue level experiments reflect changes in gene expression across multiple cell types, so it is not possible to identify which changes might originate from VSMCs vs. other cell types. To provide some insight into this question, we asked whether significantly changed genes identified in our qPCR studies were changed in our previously published in vitro RNAseq data set in which primary cultured rat microvascular VSMCs were

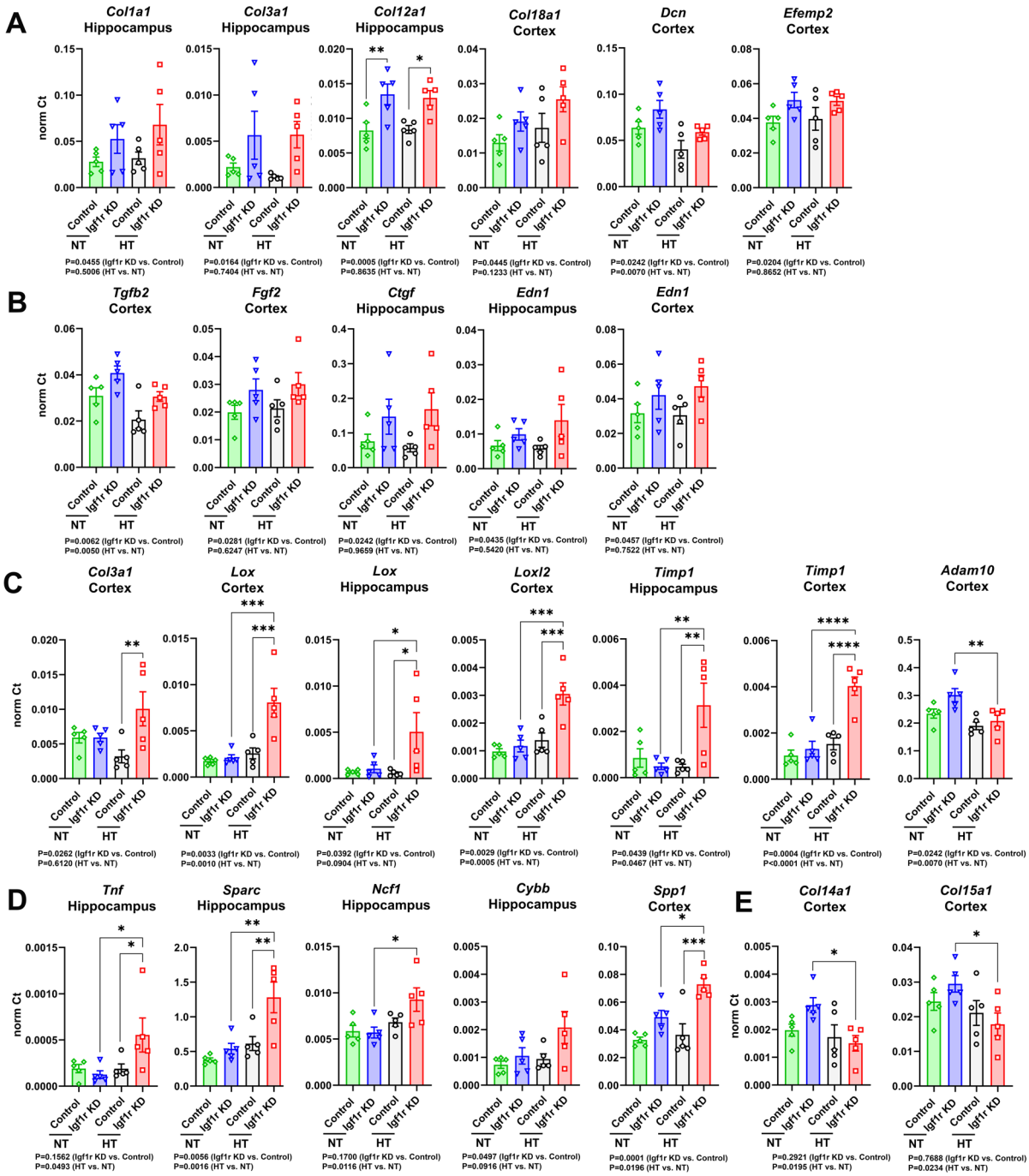

Fig. 5 VSMC-specific Igf1r KD leads to alterations in the transcription of CMH-associated genes: at day 4 after mini-pump implantation, brains from all four groups were harvested and dissected. cDNA from cortical and hippocampal tissues ($n=5$ for all groups) underwent qPCR for a panel of 96 CMH-associated genes. CT values were normalized (refer to methods). **A** and **B**. Plotted are genes upregulated in Igf1r KD animals independent of hypertension. **C** and **D**. Plotted are genes upregulated in Igf1r HT animals. E Plotted are genes downregulated in Igf1r HT animals. Graphs show means ± SEM; between-group differences were analyzed by two-way ANOVA with Tukey's post hoc tests. *P*-values for two-way ANOVAs are reported underneath each graph, where post hoc tests were significant; they are indicated on the graphs with brackets, $*P<0.05$, $**P<0.01$, $****P<0.0001$ for post hoc tests

treated with IGF-1. Many of the changes we observed in VSMC-specific Igf1r KD brains were mirrored in IGF-1-treated VSMCs (i.e., genes upregulated by Igf1r KD in vivo were downregulated by IGF-1 treatment in vitro; Fig. S3A) suggesting that some of the gene changes we observed in brain extracts could be a result of impaired IGF-1 signaling on brain VSMCs. However, we also observed some ECM genes that were upregulated in IGF-1-treated cells and in Igf1r KD brains (Fig. S3B) including *Vcan, Dcn, Col3a1,* and *Col12a1,* suggesting that the role of growth factors such as IGF-1 in ECM turnover is complex.

Discussion

Here we found that CMH development was significantly accelerated in Igf1r KD hypertensive mice as compared to control hypertensive mice, and there was a much higher degree of variability in bleed number among Igf1r KD animals vs. among controls (findings in the context of our overall hypothesis are summarized in Fig. 6). However, we did not observe a statistically significant increase in total bleed number between groups. This outcome is consistent with the fact that all hypertensive mice were collected at approximately the same neurological score (Fig. S1E). Nevertheless, prior studies have shown that even with similar study removal criteria, aging and circulating IGF-1 deficiency led to not only earlier onset of CMH development (vs. young or control mice) but also more overall bleeds. This may be partly due to differences in the prevalence of CMH development in control mice in prior studies which often had a higher fraction of control hypertensive mice with no signs of bleeds compared to our study [7, 45, 50]. However, it is likely that the more mild CMH phenotype we observe in VSMC-specific Igf1r KD animals compared to circulating IGF-1 knockdown animals [7] reflects the fact that CMH in circulating IGF-1 knockdown animals arise due to defects in more than one cell type. Circulating IGF-1 deficiency has been shown to lead to pathological remodeling of the arterial wall, where IGF-1 receptor is expressed in both VSMCs and other cells in the vasculature including endothelial cells [63]. The overall vascular fragility phenotype (i.e., development of CMH) in IGF-1-deficient mice reflects contributions from both endothelial cells and VSMCs, and future studies may separately probe the role of IGF-1 in endothelial cells in the development of CMH.

The recent publication of work using a targeted laser-induced method to elicit CMH in specific vessels [53] has provided insight into how vessel of origin correlates with bleed size and shape. This work reported that capillary and venular CMH had overlapping size distributions, usually measuring less than 5,000 μm^2 in area, while arteriolar bleeds

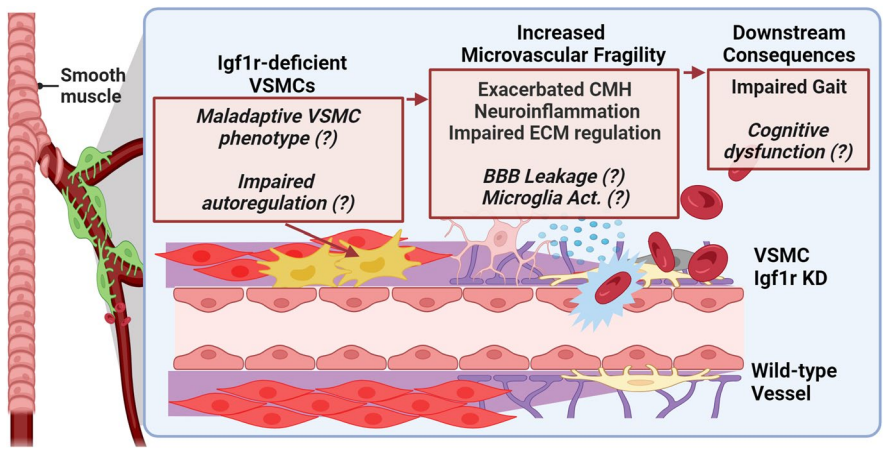

Fig. 6 Overall proposed paradigm. Show is a depiction of our overall hypothesis. We hypothesize that Igf1r deficiency in VSMCs may lead to maladaptive VSMC phenotypic switching and impaired myogenic autoregulation. As a result, we predict increased microvascular vessel fragility, resultin CMH, and other pathologies, culminating in impaired gait and cognition. Items in regular type were evaluated in this study; italicized items with (?) remain to be evaluated in future

were larger. While it is difficult to make a 1:1 correlation between hypertension-induced and laser-induced CMH, data from laser-induced CMH do provide a framework for predicting vessel of origin based on size distribution. In our study, smaller CMH (< 5,000 μm^2) were much more prevalent than larger CMH (here defined as 5,000–70,000 μm^2) in both Igf1r KD (80% of total bleeds < 5,000 μm^2) and control (73% < 5000 μm^2), suggesting that most CMH are capillary or venular in origin. The prevalence of small, likely capillary-origin, bleeds in the Igf1r KD is consistent with the idea that accelerated CMH development in Igf1r KD animals is not due to rupture of the arterioles most densely surrounded by VSMCs, but more likely due to downstream fragility in capillaries arising from impaired VSMC responses to hypertension in the absence of vasoprotective IGF-1.

Because morphology was also qualitatively correlated with vessel of origin in the laser-induced CMH model [53], we asked whether there was an accessible parameter that could be used to quantitatively assess morphology in our study. We evaluated multiple shape metrics during our bleed analysis including circularity (a measure of perimeter irregularity) and two different measures of aspect ratio (which reflects the ratio of the major axis to the minor axis of an ellipse that encircles the shape of interest). However, none of these metrics correlated well with bleed size or treatment group in our study. Given the widely varying morphologies bleeds can adopt, the overly simplistic nature of these metrics, and the inability of 2D shape descriptors to capture bleed shape in 3D, additional analysis tools will be needed to quantitatively assess bleed morphology in a meaningful way. One challenge in this study was our manual method of bleed detection and analysis of DAB-stained sections. While this method is the gold standard, the time-intensive nature limits the number of brains that can be assessed. In addition, our sampling strategy prevents 3D reconstruction of bleeds, which will be considered in future work.

One possible method to achieve 3D volumetric bleed reconstruction and evaluation could be stereological analysis which uses unbiased random histological sampling and counting to obtain quantitative information of morphometric parameters across tissue [64, 65]. Stereological analysis has been previously used for assessment of capillary lengths, numbers, and length-weighted diameters to document microvascular changes in brain regions important for hippocampal input in elderly patients across a spectrum of cognitive decline [66]. Additionally, this method was used to assess the number of neurofibrillary tangles and neurons as well as amyloid volume burden in the same areas [66]. A similar method could be applied for volumetric analysis of bleed burden in future studies to obtain an accurate 3D reconstruction of bleeds. In addition, development of supervised machine learning algorithms that enable 3D bleed reconstruction, analysis, and mapping would be of great benefit to studies aimed at understanding the factors that affect development and distribution of CMH.

Following the development of CMH in our model, we assessed alteration of gait in our mice. The presence of CMH in elderly humans has been correlated with the development of gait disturbances [14, 67, 68] and cognitive decline [12, 13]. Igf1r KD hypertensive animals exhibited impaired gait, including impaired regularity index, a measure of coordination that has been widely established to be associated with CMH [7, 46, 50]. Multiple brain regions are involved in the coordination of gait in mice and humans [7, 69]. These regions include the cerebellum [70, 71], cortex (specifically the motor cortices) [72], brainstem [73, 74], basal ganglia [75], and white matter [76]. An MRI study of patients with cerebral small vessel disease found that CMHs in the brainstem and basal ganglia were associated altered stride and step length [69]. One limitation of our studies was the comparatively small number of samples we were able to use for histological analysis of bleeds. This combined with the increased variability in bleed number in the Igf1r KD group and the brain-to-brain variability in bleed distribution meant that between-group differences in bleed distribution by region did not achieve statistical significance. However, we did observe a trend toward increased bleed number in the Igf1r KD in several regions known to be important for gait including cerebellum, brainstem, and white matter.

While we were able to study CMH and gait defects effectively using this acute hypertension paradigm, the mice had poor survival and progressed to hemorrhagic strokes if not promptly removed from the study at the first sign of neurological decline, making it difficult to evaluate CMH-associated cognitive decline. Therefore, in the future it may be beneficial to use

a less severe hypertension paradigm that induces CMH but does not progress as readily to hemorrhagic stroke. We evaluated a small cohort of animals in which angiotensin II and L-NAME were delivered as in the rest of our study, but L-NAME was withdrawn after the first 60 h (Fig. S4). These animals developed both neurological and histological signs of CMH (incidence curves again support accelerated CMH development in Igf1r KD) but did not progress to hemorrhagic stroke with the same frequency as mice who continued to receive L-NAME. A paradigm such as this one might be useful in future for studies evaluating longer-term consequences of CMH including cognitive decline and CMH clearance. This may be particularly important for increasing translational relevance as the development of CMH in aging in humans is chronic and slow, with many patients exhibiting only one or a few CMH [8, 10] rather than the larger number we see in the acute mouse model.

One of the most interesting questions to arise from this study is what the molecular mechanisms are that lead to accelerated development of CMH in VSMC-specific Igf1r KD animals. Our transcriptional studies suggest that VSMC-specific Igf1r KD elicits a complicated combination of both pro- and anti-fragility changes in gene expression. IGF-1 is largely protective in VSMCs in other models, often by suppressing the adoption of maladaptive VSMC phenotypes. There are a variety of maladaptive VSMC phenotypes seen in different tissues and pathological conditions, including pro-inflammatory macrophage/foam cell-like phenotypes, chondrogenic phenotypes associated with vessel calcification, and fibroblast-like phenotypes [19]. We found markers of all three of these phenotypes upregulated in Igf1r KD brains; *Tnf* is a marker of the macrophage-like phenotype, *Spp1* is a marker of the chondrogenic phenotype, and *Timp1* is a marker of the fibroblast-like phenotype [19].

Several of the genes altered in our experiments are also inflammatory markers. It has been well established that neuroinflammation occurs in response to CMH [77, 78], caused by both extravasation of immune cells from the blood into surrounding tissue and the activation of resident microglia and astrocytes by triggers found in extravasated blood [77, 79, 80]. However, because our transcriptional studies were performed on bulk brain tissues, it is not possible to tease out the cellular origin of any particular gene, many of which are expressed by more than one cell type. Nevertheless, our transcriptional studies do suggest a link between the neuroinflammatory landscape produced by CMH and alterations in ECM composition and turnover in VSMC-specific Igf1r KD animals. In addition to changes in some inflammatory markers, we observed an increase in the MMP inhibitor *Timp1* and a decrease in the *Adam10* protease in response to VSMC-specific Igf1r KD suggesting changes in ECM turnover. Additionally, VSMC-specific Igf1r KD results in dysregulation of collagen content (*Col3a1*, *Col14a1*, and *Col15a1*) and crosslinking (*Lox* and *Loxl2*) suggesting changes in ECM composition and stiffness.

What is not entirely clear is the directionality of these effects. A neuroinflammatory landscape can result in altered expression of genes involved ECM remodeling and secretion by VSMCs [81, 82]. However, conversely, changes in the ECM composition and turnover, regulated by VSMCs, can also trigger immune activation [83]. ECM components (coined "matrikines") from VSMCs can act as damage-associated molecular patterns interacting directly with Toll-like receptors triggering inflammatory cascades [83–85]. Additionally, ECM composition can regulate the allocation and adhesion of inflammatory cells to different regions of tissue altering immune response [86–88]. For example, microglia have been shown to perform directed migration towards stiffer environments through the process of durotaxis [89]. We look forward to future single-cell transcriptomic analyses to help delve more deeply into the cellular origins and molecular mechanisms by which Igf1r-deficient VSMCs contribute to CMH and vascular fragility.

In addition to CMH, other small lesions in the brain, such as microinfarcts, have also been implicated in the production of vascular cognitive impairment and dementia with similar risk factors such as age and hypertension [72, 90–93]. Alleles which have been shown to reduce risk for the development of intracerebral hemorrhage in the context of aging and hypertension have also been shown to reduce risk of developing microinfarcts [94, 95]. Likewise, CMH, intracerebral hemorrhage, and microinfarcts are also associated with other cerebrovascular diseases including cerebral amyloid angiopathy (CAA) and familial forms of dementia with a significant VSMC component such as cerebral autosomal dominant arteriopathy with subcortical leukoencephalopathy (CADASIL) [96, 97]. Microinfarcts and CMH have

been detected in mouse models of CADASIL [48, 98], and the co-occurrence of these two pathologies in many disease contexts suggests that microinfarcts would be an exciting area of future exploration in our model.

Since many of the signs of vascular fragility (i.e., CMH) in our model likely arise in the capillaries where VSMCs are not present, the question of how dysregulated IGF-1 signaling on VSMCs could lead to microvascular fragility is an important one. The answer may lie in the ability of VSMCs to regulate vascular tone and in particular cerebral autoregulation. This pressure-induced vasoconstriction is important to protect the cerebral microvasculature from exposure to elevated blood pressure which can lead to adverse consequences such as the development of CMH and other pathologies associated with age and hypertension [99, 100]. Support for a role for IGF-1 signaling in myogenic autoregulation comes from studies showing that circulating IGF-1 deficiency decreases vascular smooth muscle tone and impairs autoregulatory action [41], and from studies showing that increased IGF-1 levels in humans are associated with decreased incidence of hypertension [101, 102].

In addition to playing a protective role in cerebrovascular aging, IGF-1 also plays a role in other disease conditions. While there are conflicting reports from human studies, the most recent large studies suggest that IGF-1 is protective in the context of systemic cardiovascular disease, with patients with higher IGF-1 levels having reduced risk of myocardial infarction compared to those with lower IGF-1 levels, among other findings ([98] and reviewed in [103]). However, outside the vascular system, IGF-1 can be less beneficial. High IGF-1 levels have been associated with increased risk of various forms of primary and secondary cancer [104–108], likely due to the growth factor's mitogenic role. The need for balanced IGF-1 levels is highlighted by the syndromic disease experienced by patients with chronic excess or insufficient IGF-1. Acromegaly (associated with chronic overexpression of growth hormone and IGF-1) is associated with various co-morbidities including but not limited to muscle dysfunction, exaggerated growth, soft-tissue hypertrophy, and osteoarthritis [109, 110]. On the other side, people with Laron syndrome, which results in IGF-1 deficiency due to growth hormone insensitivity, have shorter life expectancies, and a cluster of symptoms including dwarfism, small cranium, and obesity [111]. Many Laron syndrome patients succumb to diseases with a vascular pathology [112], further highlighting the vasoprotective role of IGF-1.

In conclusion, this study highlights a role for VSMCs in IGF-1-associated cerebrovascular fragility, specifically the development of CMH. In our study, we see a clear association between VSMC-specific Igf1r deficiency and the development of hypertension-induced CMH and associated gait defects, modeling the phenotypes seen in elderly humans [6, 14], and highlighting VSMCs as a critical target of IGF-1-mediated vasoprotection.

Acknowledgements The authors thank Cynthia Bulmer, Morgan Johnston, and David Sherry for their technical assistance.

Author contribution Conceptualization: S. M. C., L. R. M., Z. U.; methodology: A. N. T., L. R. M., D. N.; formal analysis: S. M. C., L. R. M., M. B., M. V., T. K.; investigation: L. R. M., M. B., M. V., H. V., D. N., A. N. T., T. G., S. T., A. Y., T. K., S. M. C., E. B.; writing—original draft: L. R. M., M. B., M. V., S. M. C.; writing—review and editing: L. R. M., M. B., M. V., H. V., D. N., A. N. T., Z. U., T. G., S. T., A. Y., T. K., S. M. C., E. B.; funding acquisition: S. M. C., Z. U.; supervision: S. M. C.

Funding This work was supported by the National Institutes of Health (R01AG070915, R03AG070479, K01AG073614, R01EY019494, R01AG068295, R01AG055395) including cores supported as part of 1P20GM125528, 5P30EY021725-10, P30CA225520, and 5P30GM122744; American Heart Association (AHA941290); Hevolution Foundation, Oklahoma Shared Clinical and Translational Resources (U54GM104938); Geroscience Training Program in Oklahoma (T32AG052363); the Oklahoma Nathan Shock Center (P30AG050911); Cellular and Molecular GeroScience CoBRE (1P20GM125528); Presbyterian Health Foundation; Oklahoma Center for Adult Stem Cell Research; and the Oklahoma Center for the Advancement of Science and Technology. Funding agencies had no role in the study design; in the collection, analysis, and interpretation of data; in the writing of the report; and in the decision to submit the article for publication.

Data availability The data that support the findings of this study are available from the corresponding author upon reasonable request.

Declarations

Conflict of interest Zoltan Ungvari is the Editor-in-Chief of Geroscience. Shannon Conley, Stefano Tarantini, Adam Nyul-Toth, and Andriy Yabluchanskiy are Associate Editors of Geroscience.

References

1. Gorelick PB, Counts SE, Nyenhuis D. Vascular cognitive impairment and dementia. Biochim Biophys Acta. 2016;1862(5):860–8. https://doi.org/10.1016/j.bbadis.2015.12.015.
2. Gorelick PB, Scuteri A, Black SE, Decarli C, Greenberg SM, Iadecola C, et al. Vascular contributions to cognitive impairment and dementia: a statement for healthcare professionals from the American Heart Association/American Stroke Association. Stroke. 2011;42(9):2672–713. https://doi.org/10.1161/STR.0b013e3182299496.
3. Iadecola C, Duering M, Hachinski V, Joutel A, Pendlebury ST, Schneider JA, et al. Vascular cognitive impairment and dementia: JACC scientific expert panel. J Am Coll Cardiol. 2019;73(25):3326–44. https://doi.org/10.1016/j.jacc.2019.04.034.
4. Stokes AC, Weiss J, Lundberg DJ, Xie W, Kim JK, Preston SH, et al. Estimates of the association of dementia with US mortality levels using linked survey and mortality records. JAMA Neurol. 2020;77(12):1543–50. https://doi.org/10.1001/jamaneurol.2020.2831.
5. Fisher M, French S, Ji P, Kim RC. Cerebral microbleeds in the elderly: a pathological analysis. Stroke. 2010;41(12):2782–5. https://doi.org/10.1161/strokeaha.110.593657.
6. Ungvari Z, Tarantini S, Kirkpatrick AC, Csiszar A, Prodan CI. Cerebral microhemorrhages: mechanisms, consequences, and prevention. Am J Physiol Heart Circ Physiol. 2017;312(6):H1128–43. https://doi.org/10.1152/ajpheart.00780.2016.
7. Tarantini S, Valcarcel-Ares NM, Yabluchanskiy A, Springo Z, Fulop GA, Ashpole N, et al. Insulin-like growth factor 1 deficiency exacerbates hypertension-induced cerebral microhemorrhages in mice, mimicking the aging phenotype. Aging Cell. 2017;16(3):469–79. https://doi.org/10.1111/acel.12583.
8. Poels MM, Ikram MA, van der Lugt A, Hofman A, Krestin GP, Breteler MM, et al. Incidence of cerebral microbleeds in the general population: the Rotterdam Scan Study. Stroke. 2011;42(3):656–61. https://doi.org/10.1161/STROKEAHA.110.607184.
9. Poels MM, Ikram MA, van der Lugt A, Hofman A, Niessen WJ, Krestin GP, et al. Cerebral microbleeds are associated with worse cognitive function: the Rotterdam Scan Study. Neurology. 2012;78(5):326–33. https://doi.org/10.1212/WNL.0b013e3182452928.
10. Vernooij MW, van der Lugt A, Ikram MA, Wielopolski PA, Niessen WJ, Hofman A, et al. Prevalence and risk factors of cerebral microbleeds: the Rotterdam Scan Study. Neurology. 2008;70(14):1208–14. https://doi.org/10.1212/01.wnl.0000307750.41970.d9.
11. Ikram MA, van der Lugt A, Niessen WJ, Koudstaal PJ, Krestin GP, Hofman A, et al. The Rotterdam Scan Study: design update 2016 and main findings. Eur J Epidemiol. 2015;30(12):1299–315. https://doi.org/10.1007/s10654-015-0105-7.
12. Akoudad S, Wolters FJ, Viswanathan A, de Bruijn RF, van der Lugt A, Hofman A, et al. Association of cerebral microbleeds with cognitive decline and dementia. JAMA Neurol. 2016;73(8):934–43. https://doi.org/10.1001/jamaneurol.2016.1017.
13. Wang M, Hu H-Y, Wang Z-T, Ou Y-N, Qu Y, Ma Y-H, et al. Association of cerebral microbleeds with risks of cognitive impairment and dementia: a systematic review and meta-analysis of prospective studies. Brain Disorders. 2021;2: 100010. https://doi.org/10.1016/j.dscb.2021.100010.
14. de Laat KF, van den Berg HA, van Norden AG, Gons RA, Olde Rikkert MG, de Leeuw FE. Microbleeds are independently related to gait disturbances in elderly individuals with cerebral small vessel disease. Stroke. 2011;42(2):494–7. https://doi.org/10.1161/strokeaha.110.596122.
15. Hou Y, Yang S, Li Y, Qin W, Yang L, Hu W. Impact of cerebral microbleeds on gait, balance, and upper extremities function in cerebral small vessel disease. J Integr Neurosci. 2023;22(4):82. https://doi.org/10.31083/j.jin2204082.
16. Chai C, Wang Z, Fan L, Zhang M, Chu Z, Zuo C, et al. Increased number and distribution of cerebral microbleeds is a risk factor for cognitive dysfunction in hemodialysis patients: a longitudinal study. Medicine (Baltimore). 2016;95(12): e2974. https://doi.org/10.1097/md.0000000000002974.
17. Frismantiene A, Philippova M, Erne P, Resink TJ. Smooth muscle cell-driven vascular diseases and molecular mechanisms of VSMC plasticity. Cell Signal. 2018. https://doi.org/10.1016/j.cellsig.2018.08.019.
18. Owens GK, Kumar MS, Wamhoff BR. Molecular regulation of vascular smooth muscle cell differentiation in development and disease. Physiol Rev. 2004;84(3):767–801. https://doi.org/10.1152/physrev.00041.2003.
19. Yap C, Mieremet A, de Vries CJM, Micha D, de Waard V. Six shades of vascular smooth muscle cells illuminated by KLF4 (Kruppel-like factor 4). Arterioscler Thromb Vac Biol. 2021;41(11):2693–707. https://doi.org/10.1161/ATVBAHA.121.316600.
20. Wang Z, Ma J, Yue H, Zhang Z, Fang F, Wang G, et al. Vascular smooth muscle cells in intracranial aneurysms. Microvasc Res. 2023;149: 104554. https://doi.org/10.1016/j.mvr.2023.104554.
21. Sonntag WE, Deak F, Ashpole N, Toth P, Csiszar A, Freeman W, et al. Insulin-like growth factor-1 in CNS and cerebrovascular aging. Front Aging Neurosci. 2013;5:27. https://doi.org/10.3389/fnagi.2013.00027.
22. Chen Y, Capron L, Magnusson JO, Wallby LA, Arnqvist HJ. Insulin-like growth factor-1 stimulates vascular smooth muscle cell proliferation in rat aorta in vivo. Growth Horm IGF Res. 1998;8(4):299–303. https://doi.org/10.1016/s1096-6374(98)80125-1.
23. Bickel MA, Sherry DM, Bullen EC, Vance ML, Jones KL, Howard EW, et al. Microvascular smooth muscle cells exhibit divergent phenotypic switching responses to platelet-derived growth factor and insulin-like growth factor 1. Microvasc Res. 2023;151: 104609. https://doi.org/10.1016/j.mvr.2023.104609.
24. von der Thusen JH, Borensztajn KS, Moimas S, van Heiningen S, Teeling P, van Berkel TJ, et al. IGF-1 has plaque-stabilizing effects in atherosclerosis by altering vascular smooth muscle cell phenotype. Am J Pathol.

2011;178(2):924–34. https://doi.org/10.1016/j.ajpath.2010.10.007.
25. Shai SY, Sukhanov S, Higashi Y, Vaughn C, Kelly J, Delafontaine P. Smooth muscle cell-specific insulin-like growth factor-1 overexpression in Apoe$^{-/-}$ mice does not alter atherosclerotic plaque burden but increases features of plaque stability. Arterioscler Thromb Vac Biol. 2010;30(10):1916–24. https://doi.org/10.1161/ATVBAHA.110.210831.
26. Sukhanov S, Higashi Y, Shai SY, Snarski P, Danchuk S, D'Ambra V, et al. SM22alpha (smooth muscle protein 22-alpha) promoter-driven IGF1R (insulin-like growth factor 1 receptor) deficiency promotes atherosclerosis. Arterioscler Thromb Vac Biol. 2018;38(10):2306–17. https://doi.org/10.1161/ATVBAHA.118.311134.
27. Puche JE, Castilla-Cortázar I. Human conditions of insulin-like growth factor-I (IGF-I) deficiency. J Transl Med. 2012;10(1):224. https://doi.org/10.1186/1479-5876-10-224.
28. Ungvari Z, Csiszar A. The emerging role of IGF-1 deficiency in cardiovascular aging: recent advances. J Gerontol A Biol Sci Med Sci. 2012;67(6):599–610. https://doi.org/10.1093/gerona/gls072.
29. Breese CR, Ingram RL, Sonntag WE. Influence of age and long-term dietary restriction on plasma insulin-like growth factor-1 (IGF-1), IGF-1 gene expression, and IGF-1 binding proteins. J Gerontol. 1991;46(5):B180–7. https://doi.org/10.1093/geronj/46.5.b180.
30. Vitale G, Pellegrino G, Vollery M, Hofland LJ. Role of IGF-1 system in the modulation of longevity: controversies and new insights from a centenarians' perspective. Front Endocrinol. 2019 10. https://doi.org/10.3389/fendo.2019.00027.
31. Ashpole NM, Logan S, Yabluchanskiy A, Mitschelen MC, Yan H, Farley JA, et al. IGF-1 has sexually dimorphic, pleiotropic, and time-dependent effects on healthspan, pathology, and lifespan. Geroscience. 2017;39(2):129–45. https://doi.org/10.1007/s11357-017-9971-0.
32. Bailey-Downs LC, Mitschelen M, Sosnowska D, Toth P, Pinto JT, Ballabh P, et al. Liver-specific knockdown of IGF-1 decreases vascular oxidative stress resistance by impairing the Nrf2-dependent antioxidant response: a novel model of vascular aging. J Gerontol A Biol Sci Med Sci. 2012;67(4):313–29. https://doi.org/10.1093/gerona/glr164.
33. Bailey-Downs LC, Sosnowska D, Toth P, Mitschelen M, Gautam T, Henthorn JC, et al. Growth hormone and IGF-1 deficiency exacerbate high-fat diet-induced endothelial impairment in obese Lewis dwarf rats: implications for vascular aging. J Gerontol A Biol Sci Med Sci. 2012;67(6):553–64. https://doi.org/10.1093/gerona/glr197.
34. Fulop GA, Ramirez-Perez FI, Kiss T, Tarantini S, Valcarcel Ares MN, Toth P, et al. IGF-1 Deficiency promotes pathological remodeling of cerebral arteries: a potential mechanism contributing to the pathogenesis of intracerebral hemorrhages in aging. J Gerontol A Biol Sci Med Sci. 2019;74(4):446–54. https://doi.org/10.1093/gerona/gly144.
35. Tarantini S, Balasubramanian P, Yabluchanskiy A, Ashpole NM, Logan S, Kiss T, et al. IGF1R signaling regulates astrocyte-mediated neurovascular coupling in mice: implications for brain aging. Geroscience. 2021;43(2):901–11. https://doi.org/10.1007/s11357-021-00350-0.
36. Tarantini S, Giles CB, Wren JD, Ashpole NM, Valcarcel-Ares MN, Wei JY, et al. IGF-1 deficiency in a critical period early in life influences the vascular aging phenotype in mice by altering miRNA-mediated post-transcriptional gene regulation: implications for the developmental origins of health and disease hypothesis. Age (Dordr). 2016;38(4):239–58. https://doi.org/10.1007/s11357-016-9943-9.
37. Tarantini S, Nyul-Toth A, Yabluchanskiy A, Csipo T, Mukli P, Balasubramanian P, et al. Endothelial deficiency of insulin-like growth factor-1 receptor (IGF1R) impairs neurovascular coupling responses in mice, mimicking aspects of the brain aging phenotype. Geroscience. 2021;43(5):2387–94. https://doi.org/10.1007/s11357-021-00405-2.
38. Tarantini S, Tucsek Z, Valcarcel-Ares MN, Toth P, Gautam T, Giles CB, et al. Circulating IGF-1 deficiency exacerbates hypertension-induced microvascular rarefaction in the mouse hippocampus and retrosplenial cortex: implications for cerebromicrovascular and brain aging. Age (Dordr). 2016;38(4):273–89. https://doi.org/10.1007/s11357-016-9931-0.
39. Toth L, Czigler A, Hegedus E, Komaromy H, Amrein K, Czeiter E, et al. Age-related decline in circulating IGF-1 associates with impaired neurovascular coupling responses in older adults. Geroscience. 2022;44(6):2771–83. https://doi.org/10.1007/s11357-022-00623-2.
40. Toth P, Tarantini S, Ashpole NM, Tucsek Z, Milne GL, Valcarcel-Ares NM, et al. IGF-1 deficiency impairs neurovascular coupling in mice: implications for cerebromicrovascular aging. Aging Cell. 2015;14(6):1034–44. https://doi.org/10.1111/acel.12372.
41. Toth P, Tucsek Z, Tarantini S, Sosnowska D, Gautam T, Mitschelen M, et al. IGF-1 deficiency impairs cerebral myogenic autoregulation in hypertensive mice. J Cereb Blood Flow Metab. 2014;34(12):1887–97. https://doi.org/10.1038/jcbfm.2014.156.
42. Yan H, Mitschelen M, Toth P, Ashpole NM, Farley JA, Hodges EL, et al. Endothelin-1-induced focal cerebral ischemia in the growth hormone/IGF-1 deficient Lewis dwarf rat. J Gerontol A Biol Sci Med Sci. 2014;69(11):1353–62. https://doi.org/10.1093/gerona/glu118.
43. Toth P, Tucsek Z, Tarantini S, Sosnowska D, Gautam T, Mitschelen M, et al. IGF-1 deficiency impairs cerebral myogenic autoregulation in hypertensive mice. J Cereb Blood Flow Metabol : official J Int Soc Cereb Blood Flow Metabol. 2014;34(12):1887–97. https://doi.org/10.1038/jcbfm.2014.156.
44. Perticone F, Sciacqua A, Perticone M, Laino I, Miceli S, Care I, et al. Low-plasma insulin-like growth factor-I levels are associated with impaired endothelium-dependent vasodilatation in a cohort of untreated, hypertensive Caucasian subjects. J Clin Endocrinol Metab. 2008;93(7):2806–10. https://doi.org/10.1210/jc.2008-0646.

45. Miller LR, Tarantini S, Nyul-Toth A, Johnston MP, Martin T, Bullen EC, et al. Increased susceptibility to cerebral microhemorrhages is associated with imaging signs of microvascular degeneration in the retina in an insulin-like growth factor 1 deficient mouse model of accelerated aging. Front Aging Neurosci. 2022;14: 788296. https://doi.org/10.3389/fnagi.2022.788296.
46. Nyúl-Tóth Á, Tarantini S, Kiss T, Toth P, Galvan V, Tarantini A, et al. Increases in hypertension-induced cerebral microhemorrhages exacerbate gait dysfunction in a mouse model of Alzheimer's disease. Geroscience. 2020;42(6):1685–98. https://doi.org/10.1007/s11357-020-00256-3.
47. Available from atlas.brain-map.org. Accessed 11/14/2023.
48. Shih AY, Hyacinth HI, Hartmann DA, van Veluw SJ. Rodent models of cerebral microinfarct and microhemorrhage. Stroke. 2018;49(3):803–10. https://doi.org/10.1161/STROKEAHA.117.016995.
49. Nyul-Toth A, DelFavero J, Mukli P, Tarantini A, Ungvari A, Yabluchanskiy A, et al. Early manifestation of gait alterations in the Tg2576 mouse model of Alzheimer's disease. Geroscience. 2021;43(4):1947–57. https://doi.org/10.1007/s11357-021-00401-6.
50. Toth P, Tarantini S, Springo Z, Tucsek Z, Gautam T, Giles CB, et al. Aging exacerbates hypertension-induced cerebral microhemorrhages in mice: role of resveratrol treatment in vasoprotection. Aging Cell. 2015;14(3):400–8. https://doi.org/10.1111/acel.12315.
51. Andersen CL, Jensen JL, Orntoft TF. Normalization of real-time quantitative reverse transcription-PCR data: a model-based variance estimation approach to identify genes suited for normalization, applied to bladder and colon cancer data sets. Cancer Res. 2004;64(15):5245–50. https://doi.org/10.1158/0008-5472.CAN-04-0496.
52. Schmittgen TD, Livak KJ. Analyzing real-time PCR data by the comparative C(T) method. Nat Protoc. 2008;3(6):1101–8. https://doi.org/10.1038/nprot.2008.73.
53. Faakye J, Nyul-Toth A, Gulej R, Csik B, Tarantini S, Shanmugarama S, et al. Imaging the time course, morphology, neuronal tissue compression, and resolution of cerebral microhemorrhages in mice using intravital two-photon microscopy: insights into arteriolar, capillary, and venular origin. Geroscience. 2023. https://doi.org/10.1007/s11357-023-00839-w.
54. Mukli P, Detwiler S, Owens CD, Csipo T, Lipecz A, Pinto CB, et al. Gait variability predicts cognitive impairment in older adults with subclinical cerebral small vessel disease. Front Aging Neurosci. 2022;14:1052451. https://doi.org/10.3389/fnagi.2022.1052451.
55. Bickel MA, Csik B, Gulej R, Ungvari A, Nyul-Toth A, Conley SM. Cell non-autonomous regulation of cerebrovascular aging processes by the somatotropic axis. Front Endocrinol (Lausanne). 2023;14:1087053. https://doi.org/10.3389/fendo.2023.1087053.
56. Tan X, Li T, Zhu S, Zhong W, Li F, Wang Y. Induction of SPARC on oxidative stress, inflammatory phenotype transformation, and apoptosis of human brain smooth muscle cells via TGF-beta1-NOX4 pathway. J Mol Neurosci. 2020;70(11):1728–41. https://doi.org/10.1007/s12031-020-01566-z.
57. Li B, Li F, Chi L, Zhang L, Zhu S. The expression of SPARC in human intracranial aneurysms and its relationship with MMP-2/-9. PLoS ONE. 2013;8(3):e58490. https://doi.org/10.1371/journal.pone.0058490.
58. Zhang X, Che Y, Mao L, Li D, Deng J, Guo Y, et al. H3.3B controls aortic dissection progression by regulating vascular smooth muscle cells phenotypic transition and vascular inflammation. Genomics. 2023;115(5):110685.
59. Mori K, Okuma H, Nakamura S, Uchinuma H, Kaga S, Nakajima H, et al. Melanocortin-4 receptor in macrophages attenuated angiotensin II-induced abdominal aortic aneurysm in mice. Sci Rep. 2023;13(1):19768. https://doi.org/10.1038/s41598-023-46831-4.
60. Chen JX, Stinnett A. Critical role of the NADPH oxidase subunit p47phox on vascular TLR expression and neointimal lesion formation in high-fat diet-induced obesity. Lab Invest. 2008;88(12):1316–28. https://doi.org/10.1038/labinvest.2008.92.
61. Kuntic M, Oelze M, Steven S, Kroller-Schon S, Stamm P, Kalinovic S, et al. Short-term e-cigarette vapour exposure causes vascular oxidative stress and dysfunction: evidence for a close connection to brain damage and a key role of the phagocytic NADPH oxidase (NOX-2). Eur Heart J. 2020;41(26):2472–83. https://doi.org/10.1093/eurheartj/ehz772.
62. Fan LM, Geng L, Cahill-Smith S, Liu F, Douglas G, McKenzie CA, et al. Nox2 contributes to age-related oxidative damage to neurons and the cerebral vasculature. J Clin Invest. 2019;129(8):3374–86. https://doi.org/10.1172/JCI125173.
63. Hayes CA, Ashmore BG, Vijayasankar A, Marshall JP, Ashpole NM. Insulin-like growth factor-1 differentially modulates glutamate-induced toxicity and stress in cells of the neurogliovascular unit. Front Aging Neurosci. 2021;13:751304. https://doi.org/10.3389/fnagi.2021.751304.
64. West MJ. Design-based stereological methods for counting neurons. Progress in Brain Research. Elsevier; 2002. p. 43–51.
65. Peterson DA. Stereology. In: Kompoliti K, Metman LV, editors. Encyclopedia of movement disorders. Oxford: Academic Press; 2010. p. 168–70.
66. Bouras C, Kövari E, Herrmann FR, Rivara CB, Bailey TL, von Gunten A, et al. Stereologic analysis of microvascular morphology in the elderly: Alzheimer disease pathology and cognitive status. J Neuropathol Exp Neurol. 2006;65(3):235–44. https://doi.org/10.1097/01.jnen.0000203077.53080.2c.
67. Pinter D, Ritchie SJ, Doubal F, Gattringer T, Morris Z, Bastin ME, et al. Impact of small vessel disease in the brain on gait and balance. Sci Rep. 2017. https://doi.org/10.1038/srep41637.
68. Choi P, Ren M, Phan TG, Callisaya M, Ly JV, Beare R, et al. Silent infarcts and cerebral microbleeds modify the associations of white matter lesions with gait and postural stability: population-based study. Stroke. 2012;43(6):1505–10. https://doi.org/10.1161/strokeaha.111.647271.
69. Mao HJ, Zhang JX, Zhu WC, Zhang H, Fan XM, Han F, et al. Basal ganglia and brainstem located cerebral microbleeds contributed to gait impairment in patients with cerebral small vessel disease. J Alzheimers Dis. 2023;94(3):1005–12. https://doi.org/10.3233/JAD-230005.

70. Takakusaki K. Functional neuroanatomy for posture and gait control. J Mov Disord. 2017;10(1):1–17. https://doi.org/10.14802/jmd.16062.
71. Kiven S, Wang Y, Aich A, Argueta DA, Lei J, Sagi V, et al. Spatiotemporal alterations in gait in humanized transgenic sickle mice. Front Immunol. 2020;11: 561947. https://doi.org/10.3389/fimmu.2020.561947.
72. Graff-Radford J, Raman MR, Rabinstein AA, Przybelski SA, Lesnick TG, Boeve BF, et al. Association between microinfarcts and blood pressure trajectories. JAMA Neurol. 2018;75(2):212–8. https://doi.org/10.1001/jamaneurol.2017.3392.
73. Caggiano V, Leiras R, Goni-Erro H, Masini D, Bellardita C, Bouvier J, et al. Midbrain circuits that set locomotor speed and gait selection. Nature. 2018;553(7689):455–60. https://doi.org/10.1038/nature25448.
74. Broom L, Worley A, Gao F, Hernandez LD, Ashton CE, Shih LC, et al. Translational methods to detect asymmetries in temporal and spatial walking metrics in parkinsonian mouse models and human subjects with Parkinson's disease. Sci Rep. 2019;9(1):2437. https://doi.org/10.1038/s41598-019-38623-6.
75. Kravitz AV, Freeze BS, Parker PR, Kay K, Thwin MT, Deisseroth K, et al. Regulation of parkinsonian motor behaviours by optogenetic control of basal ganglia circuitry. Nature. 2010;466(7306):622–6. https://doi.org/10.1038/nature09159.
76. MacKinnon CD. Sensorimotor anatomy of gait, balance, and falls. Handb Clin Neurol. 2018;159:3–26. https://doi.org/10.1016/B978-0-444-63916-5.00001-X.
77. Ahn SJ, Anrather J, Nishimura N, Schaffer CB. Diverse inflammatory response after cerebral microbleeds includes coordinated microglial migration and proliferation. Stroke. 2018;49(7):1719–26. https://doi.org/10.1161/strokeaha.117.020461.
78. Wang J, Doré S. Inflammation after intracerebral hemorrhage. J Cereb Blood Flow Metab. 2007;27(5):894–908. https://doi.org/10.1038/sj.jcbfm.9600403.
79. Shtaya A, Bridges LR, Esiri MM, Lam-Wong J, Nicoll JAR, Boche D, et al. Rapid neuroinflammatory changes in human acute intracerebral hemorrhage. Annals Clin Transl Neurol. 2019;6(8):1465–79. https://doi.org/10.1002/acn3.50842.
80. Zou M, Feng Y, Xiu Y, Li Y, Zhang Y, Fan J, et al. Pertussis toxin-induced inflammatory response exacerbates intracerebral haemorrhage and ischaemic stroke in mice. Stroke Vasc Neurol. 2022;7(1):29–37. https://doi.org/10.1136/svn-2021-000987.
81. Galis ZS, Muszynski M, Sukhova GK, Simon-Morrissey E, Unemori EN, Lark MW, et al. Cytokine-stimulated human vascular smooth muscle cells synthesize a complement of enzymes required for extracellular matrix digestion. Circ Res. 1994;75(1):181–9. https://doi.org/10.1161/01.RES.75.1.181.
82. Lamb FS, Choi H, Miller MR, Stark RJ. TNFα and reactive oxygen signaling in vascular smooth muscle cells in hypertension and atherosclerosis. Am J Hypertens. 2020;33(10):902–13. https://doi.org/10.1093/ajh/hpaa089.
83. Sorokin V, Vickneson K, Kofidis T, Woo CC, Lin XY, Foo R, et al. Role of vascular smooth muscle cell plasticity and interactions in vessel wall inflammation. Front Immunol. 2020;11: 599415. https://doi.org/10.3389/fimmu.2020.599415.
84. Sorokin L. The impact of the extracellular matrix on inflammation. Nat Rev Immunol. 2010;10(10):712–23. https://doi.org/10.1038/nri2852.
85. Frevert CW, Felgenhauer J, Wygrecka M, Nastase MV, Schaefer L. Danger-associated molecular patterns derived from the extracellular matrix provide temporal control of innate immunity. J Histochem Cytochem. 2018;66(4):213–27. https://doi.org/10.1369/0022155417740880.
86. Johnson PRA, Black JL, Carlin S, Ge QI, Anne UP. The production of extracellular matrix proteins by human passively sensitized airway smooth-muscle cells in culture. Am J Respir Crit Care Med. 2000;162(6):2145–51. https://doi.org/10.1164/ajrccm.162.6.9909111.
87. Sridharan R, Cavanagh B, Cameron AR, Kelly DJ, O'Brien FJ. Material stiffness influences the polarization state, function and migration mode of macrophages. Acta Biomater. 2019;89:47–59. https://doi.org/10.1016/j.actbio.2019.02.048.
88. Atcha H, Jairaman A, Holt JR, Meli VS, Nagalla RR, Veerasubramanian PK, et al. Mechanically activated ion channel Piezo1 modulates macrophage polarization and stiffness sensing. Nat Commun. 2021;12(1):3256. https://doi.org/10.1038/s41467-021-23482-5.
89. Bollmann L, Koser D, Shahapure R, Gautier H, Holzapfel G, Scarcelli G, et al. Microglia mechanics: immune activation alters traction forces and durotaxis. Front Cellul Neurosci 2015;9.
90. Westover MB, Bianchi MT, Yang C, Schneider JA, Greenberg SM. Estimating cerebral microinfarct burden from autopsy samples. Neurology. 2013;80(15):1365–9. https://doi.org/10.1212/WNL.0b013e31828c2f52.
91. Longstreth WT Jr, Sonnen JA, Koepsell TD, Kukull WA, Larson EB, Montine TJ. Associations between microinfarcts and other macroscopic vascular findings on neuropathologic examination in 2 databases. Alzheimer Dis Assoc Disord. 2009;23(3):291–4. https://doi.org/10.1097/WAD.0b013e318199fc7a.
92. Smith EE, Schneider JA, Wardlaw JM, Greenberg SM. Cerebral microinfarcts: the invisible lesions. Lancet Neurol. 2012;11(3):272–82. https://doi.org/10.1016/s1474-4422(11)70307-6.
93. Troncoso JC, Zonderman AB, Resnick SM, Crain B, Pletnikova O, O'Brien RJ. Effect of infarcts on dementia in the Baltimore longitudinal study of aging. Ann Neurol. 2008;64(2):168–76. https://doi.org/10.1002/ana.21413.
94. Nakagawa K, Chen R, Greenberg SM, Ross GW, Willcox BJ, Donlon TA, et al. Forkhead box O_3 longevity genotype may attenuate the impact of hypertension on risk of intracerebral haemorrhage. J Hypertens. 2022;40(11):2230–5. https://doi.org/10.1097/HJH.0000000000003249.
95. Nakagawa K, Chen R, Ross GW, Donlon TA, Allsopp RC, Willcox DC, et al. FOXO3 longevity genotype attenuates the impact of hypertension on cerebral microinfarct risk. J Hypertens. 2023. https://doi.org/10.1097/HJH.0000000000003620.
96. Jouvent E, Poupon C, Gray F, Paquet C, Mangin JF, Le Bihan D, et al. Intracortical infarcts in small vessel disease: a combined 7-T postmortem MRI and

neuropathological case study in cerebral autosomal-dominant arteriopathy with subcortical infarcts and leukoencephalopathy. Stroke. 2011;42(3):e27-30. https://doi.org/10.1161/STROKEAHA.110.594218.
97. Arima H, Tzourio C, Anderson C, Woodward M, Bousser MG, MacMahon S, et al. Effects of perindopril-based lowering of blood pressure on intracerebral hemorrhage related to amyloid angiopathy: the PROGRESS trial. Stroke. 2010;41(2):394–6. https://doi.org/10.1161/STROKEAHA.109.563932.
98. Wallays G, Nuyens D, Silasi-Mansat R, Souffreau J, Callaerts-Vegh Z, Van Nuffelen A, et al. Notch3 Arg-170Cys knock-in mice display pathologic and clinical features of the neurovascular disorder cerebral autosomal dominant arteriopathy with subcortical infarcts and leukoencephalopathy. Arterioscler Thromb Vac Biol. 2011;31(12):2881–8. https://doi.org/10.1161/ATVBAHA.111.237859.
99. Chi NF, Hu HH, Chan L, Wang CY, Chao SP, Huang LK, et al. Impaired cerebral autoregulation is associated with poststroke cognitive impairment. Ann Clin Transl Neurol. 2020;7(7):1092–102. https://doi.org/10.1002/acn3.51075.
100. Toth P, Tarantini S, Csiszar A, Ungvari Z. Functional vascular contributions to cognitive impairment and dementia: mechanisms and consequences of cerebral autoregulatory dysfunction, endothelial impairment, and neurovascular uncoupling in aging. Am J Physiol Heart Circ Physiol. 2017;312(1):H1–20. https://doi.org/10.1152/ajpheart.00581.2016.
101. Vinciguerra M, Santini MP, Claycomb WC, Ladurner AG, Rosenthal N. Local IGF-1 isoform protects cardiomyocytes from hypertrophic and oxidative stresses via SirT1 activity. Aging (Albany NY). 2009;2(1):43–62. https://doi.org/10.18632/aging.100107.
102. Zhang L, Curhan GC, Forman JP. Plasma insulin-like growth factor-1 level and risk of incident hypertension in nondiabetic women. J Hypertens. 2011;29(2):229–35. https://doi.org/10.1097/HJH.0b013e32834103bf.
103. Higashi Y, Gautam S, Delafontaine P, Sukhanov S. IGF-1 and cardiovascular disease. Growth Horm IGF Res. 2019;45:6–16. https://doi.org/10.1016/j.ghir.2019.01.002.
104. Yu H, Spitz MR, Mistry J, Gu J, Hong WK, Wu X. Plasma levels of insulin-like growth factor-I and lung cancer risk: a case-control analysis. J Natl Cancer Inst. 1999;91(2):151–6. https://doi.org/10.1093/jnci/91.2.151.
105. Wu X, Zhao H, Do KA, Johnson MM, Dong Q, Hong WK, et al. Serum levels of insulin growth factor (IGF-I) and IGF-binding protein predict risk of second primary tumors in patients with head and neck cancer. Clin Cancer Res. 2004;10(12 Pt 1):3988–95. https://doi.org/10.1158/1078-0432.CCR-03-0762.
106. Ma J, Pollak MN, Giovannucci E, Chan JM, Tao Y, Hennekens CH, et al. Prospective study of colorectal cancer risk in men and plasma levels of insulin-like growth factor (IGF)-I and IGF-binding protein-3. J Natl Cancer Inst. 1999;91(7):620–5. https://doi.org/10.1093/jnci/91.7.620.
107. Hankinson SE, Willett WC, Colditz GA, Hunter DJ, Michaud DS, Deroo B, et al. Circulating concentrations of insulin-like growth factor-I and risk of breast cancer. Lancet. 1998;351(9113):1393–6. https://doi.org/10.1016/S0140-6736(97)10384-1.
108. Chan JM, Stampfer MJ, Giovannucci E, Gann PH, Ma J, Wilkinson P, et al. Plasma insulin-like growth factor-I and prostate cancer risk: a prospective study. Science. 1998;279(5350):563–6. https://doi.org/10.1126/science.279.5350.563.
109. Colao A, Grasso LFS, Giustina A, Melmed S, Chanson P, Pereira AM, et al. Acromegaly Nat Rev Dis Primers. 2019;5(1):20. https://doi.org/10.1038/s41572-019-0071-6.
110. Biagetti B, Simo R. GH/IGF-1 abnormalities and muscle impairment: from basic research to clinical practice. Int J Mol Sci. 2021;22(1). doi: https://doi.org/10.3390/ijms22010415.
111. Laron Z, Werner H. Laron syndrome — a historical perspective. Rev Endocr Metab Disord. 2021;22(1):31–41. https://doi.org/10.1007/s11154-020-09595-0.
112. Laron Z, Klinger B, Silbergeld A. Patients with Laron syndrome have osteopenia/osteoporosis. J Bone Miner Res. 1999;14(1):156–7. https://doi.org/10.1359/jbmr.1999.14.1.156.